

Protostellar Turbulence Driven by Collimated Outflows

Fumitaka Nakamura^{1,2} and Zhi-Yun Li³

ABSTRACT

The majority of stars are thought to form in clusters. Cluster formation in dense clumps of molecular clouds is strongly influenced, perhaps controlled, by supersonic turbulence. We have previously shown that the turbulence in regions of active cluster formation is quickly transformed by the forming stars through protostellar outflows, and that the outflow-driven protostellar turbulence is the environment in which most of the cluster members form. Here, we take initial steps in quantifying the global properties of the protostellar turbulence through 3D MHD simulations. We find that collimated outflows are more efficient in driving turbulence than spherical outflows that carry the same amounts of momentum. This is because collimated outflows can propagate farther away from their sources, effectively increasing the turbulence driving length; turbulence driven on a larger scale is known to decay more slowly. Gravity plays an important role in shaping the turbulence, generating infall motions in the cluster forming region that more or less balance the outward motions driven by outflows. The resulting quasi-equilibrium state is maintained through a slow rate of star formation, with a fraction of the total mass converted into stars per free fall time as low as a few percent. Magnetic fields are dynamically important even in magnetically supercritical clumps, provided that their initial strengths are not far below the critical value for static cloud support. They contain an energy comparable to the turbulent energy of the bulk cloud material, and can significantly reduce the rate of star formation. We find that the mass weighted probability distribution function (PDF) of the volume density of the protostellar turbulence is often, although not always, approximately lognormal. The PDFs of the column density deviate more strongly from lognormal distributions. There is a prominent break

¹Faculty of Education and Human Sciences, Niigata University, 8050 Ikarashi-2, Niigata 950-2181, Japan; fnakamur@ed.niigata-u.ac.jp

²Visiting Astronomer, Division of Theoretical Astrophysics, National Astronomical Observatory, Mitaka, Tokyo 181-8588, Japan

³Department of Astronomy, University of Virginia, P. O. Box 400325, Charlottesville, VA 22904; zl4h@virginia.edu

in the velocity power spectrum of the protostellar turbulence, which may provide a way to distinguish it from other types of turbulence.

Subject headings: ISM: clouds — ISM:magnetic fields — MHD — stars: formation — turbulence

1. Introduction

We investigate the role of protostellar outflows in cluster formation. The formation of stellar clusters is important to study for at least two reasons. First, the majority of stars are thought to form in clusters (Lada & Lada 2003; Allen et al. 2006). This follows from the observations that most stars are born in giant molecular clouds (GMCs) and that in nearby GMCs such as the Orion molecular clouds where systematic surveys are available the majority of young stellar objects are found in clusters. Just as importantly, it is in clusters that most, if not all, massive stars are produced. Understanding cluster formation is likely a prerequisite to understanding massive star formation.

Outflows play an important role in star formation in general and cluster formation in particular. Individually, they may drive the accretion in the inner disk (Königl & Pudritz 2000), brake the stellar rotation (Shu et al. 2000), and perhaps help defining the most fundamental quantity of a star—the mass (Nakano et al. 1995; Matzner & McKee 2000; Shu et al. 2004). Collectively, they have the potential to replenish the energy and momentum dissipated in a star-forming cloud. This possibility was first examined in detail by Norman & Silk (1980). They envisioned the star-forming clouds to be constantly stirred up by the winds of optically revealed T Tauri stars. The idea was strengthened by the discovery of molecular outflows (McKee 1989), which point to even more powerful outflows from the stellar vicinity during the embedded, *protostellar* phase of star formation (Lada 1985; Bontemps et al. 1996). Shu et al. (1999) estimated the momentum output from protostellar outflows based on the Galactic star formation rate, and concluded that it is sufficient to sustain in all molecular gas a level of turbulence at $\sim 1 - 2$ km/s, not far from the line widths actually observed in typical GMCs. If the majority of stars are formed in localized parsec-scale dense clumps that occupy a small fraction of the GMC volume (Lada et al. 1991), their ability to influence the dynamics of the bulk of the GMC material will probably be reduced; other means of turbulence maintenance may be needed in regions of relatively little star formation, as concluded by Walawender et al. (2005) in the case of the Perseus molecular cloud. The concentration of star formation should, however, make the outflows more important in the spatially limited, but arguably the most interesting, regions of a GMC—the regions of cluster formation, where the majority of stars are thought to form.

We have made a start in simulating cluster formation in magnetized parsec-scale dense clumps including outflows (Li & Nakamura 2006). We find that, in agreement with previous work (Mac Low et al. 1998; Stone et al. 1998; Padoan & Nordlund 1999), the initial turbulence that the clump inherits from its formation process decays away quickly. It is replaced by the motions driven by the protostellar outflows associated with star formation. It is in this protostellar outflow-driven turbulence (“protostellar turbulence” for short hereafter) that the majority of the cluster members are produced. In this picture, quantifying the protostellar turbulence becomes a pressing issue. The current investigation is a step in this direction.

An important issue that we seek to address is how fast stars form in a cluster. The star formation rate (SFR) can be constrained by observations. For example, Lada et al. (1996) derived an average SFR of $\dot{M}_* \approx 4.5 \times 10^{-5} M_\odot \text{ yr}^{-1}$ for the nearby embedded cluster associated with the reflection nebula NGC 1333 in the Perseus molecular cloud, based on an estimate of the total stellar mass ($\sim 45 M_\odot$) and the duration of star formation ($\sim 10^6$ years; see also Aspin 2003). It is to be compared with the limiting rate expected in the case of unimpeded star formation (where most of the cloud mass is converted into stars in one free-fall time)

$$\dot{M}_{\text{ff}} = \frac{M}{\bar{t}_{\text{ff}}} = \left(\frac{32G}{3\pi} \right)^{1/2} \left(\frac{M}{L} \right)^{3/2} = 3.91 \times 10^{-3} \left(\frac{M}{10^3 M_\odot} \right)^{3/2} \left(\frac{1\text{pc}}{L} \right)^{3/2} M_\odot \text{yr}^{-1}, \quad (1)$$

where M and L are the mass and size of the region, and \bar{t}_{ff} is the free-fall time at the average density $\bar{\rho} = M/L^3$. In the case of NGC 1333, Warin et al. (1996) carried out a detailed mapping of the molecular gas in ^{13}CO and C^{18}O , and estimated a mass of $2900 M_\odot$ from ^{13}CO and $950 M_\odot$ from C^{18}O in an area of 650 arcmin^2 , corresponding to a size $L = 2.60 \text{ pc}$ for an adopted distance of 350 pc . The two masses yield $\dot{M}_{\text{ff}} = 4.62 \times 10^{-3}$ and $8.66 \times 10^{-4} M_\odot \text{ yr}^{-1}$, respectively. For a smaller core region of 140 arcmin^2 in area (or $L = 1.20 \text{ pc}$), a mass of $450 M_\odot$ is estimated from C^{18}O , yielding $\dot{M}_{\text{ff}} = 8.93 \times 10^{-4} M_\odot \text{ yr}^{-1}$. Note that the values of SFR from C^{18}O are comparable on the two scales; the decrease in mass for the core is nearly offset by a decrease in size. These three values of \dot{M}_{ff} are some 20-100 times larger than the actual SFR inferred by Lada et al. (1996). Unless most stars in the NGC 1333 cluster form within a period of time much shorter than 10^6 years (which is not supported by the presence of relatively evolved Class II YSOs and the detailed analyses of Lada et al. [1996] and Aspin [2003], although a mini-burst of star formation involving a fraction of the stars, particularly Class 0 objects, appears to be ongoing in this deeply embedded cluster [Bally et al. 1996]), the SFR must be reduced by at least an order of magnitude below the free-fall value in order to match observations. This conclusion is strengthened by the recent HCO^+ and N_2H^+ observations of Walsh et al. (2006), which yield a cluster-wide mass accretion rate of order $10^{-4} M_\odot \text{ yr}^{-1}$. The rate is comparable to the star formation rate \dot{M}_* and much

lower than the free-fall rate \dot{M}_{ff} .

The ratio of the actual to limiting star formation rates, $\dot{M}_*/\dot{M}_{\text{ff}}$, has a simple physical meaning: the fraction of the cloud mass turned into stars in one free-fall time. It is the dimensionless star formation rate SFR_{ff} defined in Krumholz & McKee (2005) and Krumholz & Tan (2006). The latter authors estimated values of a few percent for $\text{SFR}_{\text{ff}} = \dot{M}_*/\dot{M}_{\text{ff}}$ in three types of objects of different characteristic densities, including giant molecular clouds, infrared dark clouds, and Galactic and extragalactic dense gas traced by HCN. The values, while uncertain, are compatible with the range that we estimated above ($\sim 1\% - 5\%$) for NGC 1333. The small values for SFR_{ff} imply that star formation does not proceed at the limiting free-fall rate in molecular clouds in general (Zuckerman & Evans 1974) and localized cluster-forming regions in particular. It must be retarded somehow.

Cluster formation may be retarded by magnetic fields. The magnetic field is particularly well observed in OMC1—the nearest region of ongoing massive star formation. It has a hourglass shape (produced perhaps by gravitational contraction; Schleuning 1998; Houde et al. 2004), a line-of-sight field strength of $360 \pm 80 \mu\text{G}$ from CN Zeeman measurements (Crutcher 1999). If we adopt an inclination angle of the field line of $\vartheta = 65^\circ$ to the line of sight determined by Houde et al. (2004), the total field strength would become $\sim 850 \mu\text{G}$, which would imply a global magnetic flux-to-mass ratio ~ 2.6 times below the critical value for cloud support by a static magnetic field. The ratio was estimated based on the column density measured along the line of sight, which should be higher than the column density along the minor axis of the (elongated) clump. Correcting for this projection effect would bring the intrinsic flux-to-mass ratio closer to the critical value. Crutcher (2005) reviewed the available observational data on other regions of cluster/massive star formation and concluded that their magnetic fields, when detected, appear to have strengths not far from the critical values as well. We are thus motivated to include in our simulations moderately strong magnetic fields, with strengths up to half of the critical value. We do not consider magnetically subcritical clouds, where star formation is enabled by ambipolar diffusion, a process not treated in the present paper.

Supersonic turbulence can also slow down (global) star formation. A major concern is that the turbulence tends to decay quickly, even in the presence of a strong magnetic field (e.g., Mac Low et al. 1998; Stone et al. 1998; Padoan & Nordlund 1999). Unless the cloud is short-lived, the observed supersonic turbulence must be replenished. A common practice is to drive the turbulence in Fourier space. The extent to which such a treatment is adequate for the turbulence observed in molecular clouds remains to be ascertained (e.g., Elmegreen & Scalo 2004). In particular, it is unclear whether the treatment is applicable to the turbulence in regions of active cluster formation, which we have argued previously has a

unique origin: it is driven from within by protostellar outflows accompanying star formation (Li & Nakamura 2006; see also Cunningham et al. 2006 and Matzner 2007). The goal of the paper is to quantify this outflow-driven turbulence and the rate of star formation in it through numerical simulation.

The rest of the paper is organized as follows. In § 2, we describe the formulation of the physical model, including the simulation setup and numerical code used. The results of the simulations are presented in § 3 and § 4. We discuss the results and their implications in § 5, and summarize our main conclusions in § 6.

2. Model Formulation

2.1. Initial and Boundary Conditions

We consider a self-gravitating cloud in a cubic box of length L on each side. Standard periodic conditions are imposed at the boundaries. As in Li & Nakamura (2006), we choose an initial density distribution that is centrally condensed. The distribution is motivated by the fact that embedded clusters, such as NGC 1333 (Ridge et al. 2003) and the Serpens core (Olmi & Testi 2002), are often surrounded by envelopes with density decreasing away from the cluster. Compared with the oft-used uniform density distribution, it has the advantage of better isolating the central region of active cluster formation gravitationally from its mirror images introduced by the periodic boundary condition. The adopted functional form for the density profile is

$$\rho(r) = \begin{cases} \frac{\rho_0}{1 + (r/r_0)^2}, & r \leq r_e = L/2 \\ \frac{\rho_0}{1 + (r_e/r_0)^2}, & r > r_e = L/2 \end{cases} \quad (2)$$

where ρ_0 is the peak density at the center and r the spherical radius. The two characteristic radii, r_0 and r_e , measure the sizes of the central plateau region and the cloud as a whole. We adopt $r_0 = r_e/3$, corresponding to a central-to-edge density contrast of 10. The density in the region between the cubic simulation box and the sphere of radius r_e is held constant.

To ensure that the cloud contains many Jeans masses for fragmentation into a cluster, we choose a size for the simulation box that is 9 times the Jeans length at the cloud center

$$L_J = (\pi c_s^2 / G \rho_0)^{1/2}. \quad (3)$$

The isothermal sound speed $c_s = 2.66 \times 10^4 (T/20K)^{1/2}$ cm/s, where T is the cloud temperature, and the central density $\rho_0 = 4.68 \times 10^{-24} n_{H_2,0}$ g cm⁻³, with $n_{H_2,0}$ being the central number density of molecular hydrogen, assuming 1 He for every 10 H atoms. We adopt a

fiducial value $L = 1.5$ pc, typical of the dimensions of cluster-forming clumps. It corresponds to a Jeans length $L_J = L/9 = 0.17$ pc. Scaling the box size L by 1.5 pc, we obtain a central number density,

$$n_{H_2,0} = 2.69 \times 10^4 \left(\frac{T}{20K} \right) \left(\frac{1.5\text{pc}}{L} \right)^2 \text{cm}^{-3}, \quad (4)$$

and a total cloud mass,

$$M_{\text{tot}} = 9.39 \times 10^2 M_{\odot} \left(\frac{T}{20K} \right) \left(\frac{L}{1.5\text{pc}} \right) \quad (5)$$

inside the computation domain. The mass is also typical of the nearby cluster-forming clumps for the fiducial parameters (e.g., Ridge et al. 2003).

From the Jeans length and sound speed, we define a gravitational collapse time

$$t_g = \frac{L_J}{c_s} = 6.12 \times 10^5 \left(\frac{L}{1.5\text{pc}} \right) \left(\frac{20K}{T} \right)^{1/2} \text{(years)}. \quad (6)$$

It is longer than the free fall time at the cloud center

$$t_{\text{ff}} = \left(\frac{3\pi}{32G\rho_0} \right)^{1/2} = 1.88 \times 10^5 \left(\frac{L}{1.5\text{pc}} \right) \left(\frac{20K}{T} \right)^{1/2} \text{(years)}, \quad (7)$$

by a factor of 3.27. The time t_g is 26% longer than the free fall time \bar{t}_{ff} at the average cloud density $\bar{\rho} = 0.15\rho_0$.

We impose a uniform magnetic field along the x axis at the beginning of simulation. The field strength is specified by the parameter α , the ratio of magnetic to thermal pressure at the cloud center, through

$$B_0 = 4.73 \times 10^{-5} \alpha^{1/2} \left(\frac{T}{20K} \right) \left(\frac{1.5\text{pc}}{L} \right) \text{(Gauss)}. \quad (8)$$

In units of the critical value $2\pi G^{1/2}$ (Nakano & Nakamura 1978), the flux-to-mass ratio in the central flux tube is

$$\Gamma_0 = \frac{2^{1/2} \alpha^{1/2}}{3\pi \tan^{-1}(r_e/r_0)} = 0.12\alpha^{1/2}. \quad (9)$$

The dimensionless flux-to-mass ratio for the cloud as a whole is $\bar{\Gamma} = 0.33\alpha^{1/2}$, which is nearly three times larger than the central value. The envelope is more strongly magnetized than the central region.

In addition to the magnetic field, we include in our simulation a modest level of rotation. Although slow rotation is generally difficult to measure in a strongly turbulent cluster-forming environment, it has been claimed in some cases, such as the Serpens core (Olmi &

Testi 2002). The inferred level of rotation is typically not high enough to prevent the collapse of the cloud as a whole. It could become more important on smaller scales. We assume that the clump rotates slowly around the z axis (perpendicular to the initial magnetic field lines), with a profile

$$V_{\text{rot}} = \begin{cases} \frac{3(\varpi/r_0)c_s}{1 + (\varpi/r_0)^2}, & \varpi < r_e \\ 0, & \varpi \geq r_e \end{cases} \quad (10)$$

where ϖ is the distance from the rotation axis that passes through the center of the simulation box. The rotation speed peaks at a cylindrical radius $\varpi = r_0 = L/6$, with a maximum value of $1.5c_s$. It is set to zero at the simulation boundaries to satisfy the periodic condition. This distribution of rotation speed is used in all simulations.

We stir the cloud at the beginning of the simulation with a turbulent velocity field of power spectrum $v_k^2 \propto k^{-3}$ and a mass weighted rms Mach number $\mathcal{M} = 10$. Following the standard practice (e.g., Ostriker et al. 2001), random realization of the power spectrum is done in Fourier space. The turbulence is allowed to decay freely, except for the feedback from protostellar outflows. We have experimented with other choices for the initial turbulence, including different random realizations of the same power spectrum and different power-laws for the spectrum (e.g., $v_k^2 \propto k^{-1}, k^{-2}$, and k^{-4}), and obtained qualitatively similar results. In particular, the fully developed protostellar turbulence is insensitive to the variations in the initial turbulence.

2.2. Prescriptions for Stellar Mass and Outflow

How the mass of a star is determined is a long-standing, unresolved problem. Low-mass stars are observed to form in dense cores of molecular clouds. There is evidence that only a fraction of the core material eventually ends up inside stars. For example, Onishi et al. (2002) derived an average virial mass of about $5M_\odot$ for the H^{13}CO^+ cores in the Taurus molecular clouds. This mass is an order of magnitude higher than that of a typical star formed in the region, which is only $\sim 0.5 M_\odot$ (Kenyon & Hartmann 1995). Dense cores in more crowded cluster-forming regions are more difficult to resolve observationally. They may convert a higher fraction of their mass into stars (Motte et al. 1998), although this is uncertain. In regions far from massive stars, the masses of low-mass stars are probably determined by the competition between protostellar infall and outflow, neither of which is fully understood. In our treatment, we will leave the stellar mass as a quantity to be prescribed.

To specify the stellar mass, we adopt the following recipe for mass extraction. When

the density in a cell crosses a threshold $\rho_{\text{th}} = 100\rho_0$, we define around it a “supercell” that includes all cells in direct contact with the central cell, either through a surface, a line or a point. The supercell is thus a cubic region having 3 cells on each side and 27 cells in total. From each of the 27 cells, we extract 20% of the mass and put it in a Lagrangian particle located at the supercell center; the particle represents a formed “star.” The percentage of the mass extracted is chosen to yield a stellar mass $M_* \approx 0.5 M_\odot$, typical of low mass stars. We have examined the physical conditions of the gas in a large number of supercells, and found the gas to be self-gravitating and well on the way to star formation. At formation, we assume that the star moves with the velocity of its host cell. Its subsequent evolution through the cluster potential, which includes contributions from both gas and stars¹, is followed numerically.

Following Matzner & McKee (2000), we assume that each star injects into the ambient medium a momentum that is proportional to the stellar mass M_* . We denote the proportionality constant by P_* , and normalize it by 100 km/s. In the Appendix, we find a likely range for the scaled outflow parameter $f = P_*/100$ km/s between ~ 0.1 and ~ 1 . We will adopt $f = 0.5$ as our fiducial value, corresponding to a round number $P_* = 50$ km/s, which is close to the value 40 km/s adopted by Matzner & McKee (2000) in their semi-analytic model of cluster formation. For comparison, we will also discuss in some depth a simulation with weaker outflows specified by $P_* = 25$ km/s.

We assume that the outflow momentum M_*P_* ejected by a star of mass M_* is shared instantaneously by the material left in the supercell immediately after the stellar mass extraction. This prescription is similar to the one used by Allen & Shu (2000) in their simulation of outflow-driven motions in critically magnetized, sheet-like GMCs. In our initial study (Li & Nakamura 2006), we let the momentum-carrying material in the supercell move radially away from the center, with the same speed in all directions. However, there is ample observational evidence and strong theoretical arguments for the protostellar outflows being collimated in general (Bachiller & Tafalla 1999; Shu et al. 1995). Here, we go beyond the simplest prescription, and adopt a two-component structure for the outflow, with each component serving a distinct purpose: a collimated, “jet” component that facilitates the energy and momentum transport to large distances, surrounded by a spherical component that reverses the local infall after a star is formed. As in Allen & Shu (2000), we pick the direction of the magnetic field in the central cell as the jet axis. Included in the jet component are all cells of the supercell whose centers lie within 30° of the axis; the remaining cells are assigned to the spherical component. The jet carries a fraction η of the total outflow momentum

¹In computing the contribution of a formed star (or Lagrangian particle) to the gravitational potential, we spread its mass evenly in its host cell to avoid singularity.

M_*P_* ; the remaining fraction is carried by the spherical component. The material in each component is driven away from the center radially, with a speed given by the momentum divided by the mass in that component.

The above prescriptions for stellar mass and outflow, while idealized, serve as a reasonable first approximation in our view. Possible future refinements are described in § 5.3.

2.3. Numerical Code

The MHD equations that govern the cloud evolution are solved using a 3D MHD code based on an upwind TVD scheme. To ensure that the magnetic field is divergence free, we replace the magnetic field \mathbf{B} by $\mathbf{B}^{\text{new}} = \mathbf{B} - \nabla\Phi_B$ (where $\nabla^2\Phi_B = \nabla \cdot \mathbf{B}$) after each time step. The code does not contain any artificial viscosity, which allows the shocks to be captured sharply. We have tested the code against standard shock tube problems and the problem of point explosion. The tests show that our code is second-order accurate in both space and time, and that it suppresses a numerical instability that appears just behind a shock front for non-TVD code like the Lax-Wendroff code [see e.g., Fig. 7 of Nakamura et al. (1999) and Fig. 7 of Nakamura (2000)]. The 3D code is an extension of the well-tested 2D codes that we have used in several previous studies (e.g., Nakamura et al. 1999 and Li & Nakamura 2002).

We solve the Poisson equation for gravitational potential using fast Fourier transform, taking advantage of the periodic boundary conditions imposed. As is the standard practice, we set the $k = 0$ component of the gravitational potential to zero in Fourier space. This is equivalent to using $\rho - \bar{\rho}$ (where $\bar{\rho}$ is the mean density of the cloud), rather than ρ , as the source term in the Poisson equation. Formed stars are treated separately from the gas, as Lagrangian particles. Their equations of motion are solved using a symplectic method.

In the simulations to be presented in this paper, we adopt a uniform grid of 128^3 . This resolution is relatively low compared to some recent simulations of MHD turbulence in molecular clouds (e.g., Li et al. 2004). However, our simulations include a new ingredient—protostellar outflows—and are followed to a time significantly later than the previous simulations. Both the outflow and longer evolution exacerbate the time step problem associated with large Alfvén speeds in rarefied regions. Restricting ourselves to a relatively modest resolution allows us to carry out an exploration of parameters essential to the problem. Furthermore, our grid does contain more than 2 million cells, which enable us to resolve the global structure of the outflow-driven turbulence reasonably well. We are running a couple of higher resolution simulations with 256^3 . Preliminary analyses show that our main results

do not depend sensitively on resolution.

3. Protostellar Outflow-driven Turbulence: the Standard Model

A number of parameters are needed to fully specify our simulations. In this paper, we will concentrate on three that most directly affect the properties of the protostellar outflow-driven turbulence. These include the parameters f and η , which characterize the strength and collimation of the outflow respectively, and the ratio of magnetic-to-thermal energy at the cloud center α , which specifies the degree of cloud magnetization. Other parameters, such as those specifying the initial mass distribution and turbulent velocity field, are kept fixed to facilitate model comparison. In this section, we focus on a “standard” model with $\alpha = 2.5$, $f = 0.5$ and $\eta = 0.75$ (Model S0 in Table 1). The choice $\alpha = 2.5$ yields a dimensionless flux-to-mass ratio of 0.19 (in units of the critical value $2\pi G^{1/2}$) in the central flux tube and 0.52 for the cluster-forming clump as a whole. The clump is therefore magnetically supercritical, although only moderately so for the bulk of the cloud material. The choice $f = 0.5$ corresponds to a relatively strong outflow, and $\eta = 0.75$ means that the outflow momentum is dominated by the relatively narrow “jet” component. The combination of model parameters is chosen to yield a relatively low rate of star formation. This simulation will serve as the standard against which other simulations, listed in Table 1 and to be discussed in the next section, are compared.

3.1. Star Formation Rate

One of the most important quantities of cluster formation is the star formation efficiency (SFE hereafter), defined as the ratio of the mass of all stars to the total mass of stars and gas. It determines, among other things, whether a cluster would remain gravitationally bound upon gas removal. In Fig. 1, we plot the SFE of the standard model as a function of time, in units of the gravitational time t_g , which is 26% longer than the average free-fall time \bar{t}_{ff} . The first several stars form in quick succession around $0.4 t_g$, followed by a period of relative quiescence. Episodes of similar mini-bursts of star formation are also evident at later times. By the last time shown in Fig. 1 ($t = 2 t_g$ or $1.22[L/1.5\text{pc}][20K/T]^{1/2}$ Myrs), a total of 114 stars have formed, with an accumulative SFE of $\sim 6\%$. The average mass of a star is $\sim 0.5 M_{\odot}(T/20K)(L/1.5\text{pc})$, typical of low-mass stars, as mentioned earlier. From the fact that within a time interval $\sim 1.6 t_g$ (or $\sim 2 \bar{t}_{\text{ff}}$) since the formation of the first star $\sim 6\%$ of the gas has been converted into stars, we obtain a star formation efficiency per free-fall time $\text{SFR}_{\text{ff}} \approx 3\%$. It is in the range of star formation rate inferred for the embedded cluster NGC

1333 and other types of objects (see discussion in § 1). At this rate, it takes some 33 free-fall times to completely deplete the gas in the cluster forming region through star formation². To understand why the star formation is slowed down to such a remarkable extent, we examine in some depth the internal structure and dynamics of the cluster-forming clump, starting from global quantities such as the total energy and momentum. The effects of the magnetic field are discussed separately in the next section (§ 4.3).

3.2. Evolution of Scalar Momentum and Gravitational Energy

The momentum is more useful to keep track of than the kinetic energy in our standard simulation. This is because the kinetic energy can easily be dominated by the fast moving outflows, especially the jet components. Impulsive injection and rapid dissipation of the outflow energy generate large variations in the total kinetic energy, even though the kinetic energy of the bulk cloud material away from the active outflows remains relatively constant. The total (scalar) momentum is not expected to vary as strongly, since the outflows interact with the ambient medium in a momentum-conserving fashion. In Fig. 2, we show the evolution of the total (scalar) momentum divided by the total mass of the gas. The ratio is the specific momentum or simply the mass-weighted turbulent speed, which we will denote by v_{turb} . It provides a better measure of the turbulent speed of the bulk material than the oft-used mass-weighted rms velocity; the latter is more dominated by active outflows. As expected, the specific momentum decreases rapidly at the beginning of the simulation, as a result of the momentum-canceling (head-on) collisions that develop in the highly compressive initial turbulent velocity field. The decline is stopped by the formation of stars, whose outflows appear to have kept the turbulent speed v_{turb} close to $\sim 5 c_s$ at late times. The near constancy of v_{turb} indicates that the turbulent gas has reached a quasi-equilibrium state.

The specific momentum of the turbulent gas is to be compared with the specific momentum injected into the gas by outflows. The latter is given by $v_{\text{inj}} = M_{*,\text{tot}} P_*/M_{\text{gas}}$, where $M_{*,\text{tot}}$ and M_{gas} are the total masses of the stars and gas, respectively, and P_* is the outflow momentum per unit stellar mass. If only a small fraction of the gas is converted into stars, as in the standard simulation, we have $v_{\text{inj}} \approx \text{SFE} \times P_*$, where SFE is the star formation efficiency. For the adopted $P_* = 50 \text{ km/s}$, we have $v_{\text{inj}} \approx 3 \text{ km/s}$ at the end of the simulation ($2 t_g$), when $\text{SFE} \approx 6\%$. It is about twice the mass-weighted turbulent speed $v_{\text{turb}} \approx 1.5 \text{ km/s}$ at the same time. In Fig. 2, we show the speed v_{inj} as a function of time along with the

²It does not mean that the clump will live for a time as long as the depletion time. The clump will likely be dispersed either internally or externally long before the conversion of gas to stars is completed.

turbulent speed v_{turb} . From the slope of the v_{inj} curve, we estimate the amount of specific momentum injected into the cloud by outflows per gravitational time t_g to be $\sim 7 c_s$. At this rate, it takes $\sim 0.7 t_g$ (or $\sim 0.9 \bar{t}_{\text{ff}}$) to replenish the equilibrium specific momentum $v_{\text{turb}} \approx 5 c_s$. In a steady state, this should also be the momentum dissipation time.

Another indication that a quasi-equilibrium state is reached at late times comes from the evolution of the absolute value of the gravitational energy³ per unit mass, E_g , shown in Fig. 3. The initial increase in E_g is caused by turbulence dissipation, which leads to cloud contraction, starting from an initial mass distribution that is already somewhat centrally condensed. The contraction is slowed down, and eventually arrested by the outflows associated with star formation. The near constancy of the gravitational energy at late times implies that the system is neither collapsing nor expanding rapidly as a whole. It signals that a quasi-equilibrium state has been reached. In what follows, we shall examine in some detail the structure and dynamics of the quasi-equilibrium state, focusing on a representative time $1.5 t_g$, when 80 stars have formed and the outflow-driven protostellar turbulence appears fully developed.

3.3. Quasi-Equilibrium State

Global quantities such as the total scalar momentum and gravitational energy do not capture the full complexity of the gas dynamics. This complexity is illustrated in Fig. 4, where we show a color map of the density distribution, with velocity vectors and contours of the gravitational potential superposed. Naively, one might expect the gas to slide down the gravitational potential well towards the bottom more or less freely, producing an infall-dominated velocity field that leads to rapid star formation at the limiting free-fall rate given by equation (1). Infall motion does appear in some regions, but not in others: many patches have more or less coherent motions in directions around or away from the bottom of the potential well. The patchy appearance of the velocity field is a general feature of the protostellar turbulence that we also see at other times and in other simulations. The patches are often separated by regions of enhanced density, which are probably created by converging flows. An important question is: are the infall and outflow motions more or less balanced globally so as to keep the self-gravitating system close to a dynamical equilibrium?

To address the above question quantitatively, we show in Fig. 5 the mass weighted

³We remind the reader that the $k = 0$ component of the gravitational potential is set to zero in Fourier space to accommodate the periodic boundary condition. This treatment reduces the absolute value of the gravitational energy in the model compared to the case where the cloud exists in isolation.

probability distribution function (PDF) for the radial component of the velocity, v_r , towards or away from the location of minimum gravitational potential. The PDF peaks around $v_r \approx -1 c_s$, and a simple integration yields that 61% of the total mass has a negative radial velocity and is thus infalling. The outflowing gas moves somewhat faster on average, however. If we define an average infall (outflow) speed from the total inward (outward) momentum divided by the total infalling (outflowing) mass, we obtain a value of $3.99 c_s$ for outflow and $-2.40 c_s$ for infall. The faster outflow speed is consistent with the fact that the PDF shows a stronger wing towards positive v_r . The *net* radial velocity, defined as the *net* total radial momentum divided by the total mass, is only $0.08 c_s$, much smaller than either the average infall or outflow speed. It is only a small fraction of the sound speed, indicating the outflow and infall motions are nearly balanced globally, leaving the system in a rough, dynamical equilibrium in the radial direction. The balance is generally true at other times as well, although the net radial speed can go up to several tenths of the sound speed.

3.4. Mass Distribution

It is well known that supersonically turbulent media are clumpy, with a wide range of densities. In Fig. 6(a), we plot the mass weighted PDF for the volume density at the representative time. The distribution appears roughly lognormal, peaking around $\sim 0.6 \rho_0$ (or ~ 4 times the average density), broadly consistent with previous simulations (e.g., Ostriker et al. 2001), despite the fact that in our simulation the supersonic turbulence is created and maintained in a potential well of considerable depth and gravity plays a more dominant role. There is some deviation at the high density end, where the PDF is dominated by dense cores and filaments, some of which are self-gravitating and are on the verge of collapse to form a new generation of stars. In Fig. 6(b), we plot the fraction of the total mass that resides in regions above a given density. At low densities, the mass fraction asymptotes to a value slightly below unity, because a few percent of the mass has already been converted into stars at the time under consideration. It decreases quickly towards the high density end. Only 12% of the mass resides in regions denser than $5 \rho_0$, and this fraction drops to 5.8% above $10 \rho_0$. The rapid decrease in the amount of mass available for star formation towards the high density end is a key ingredient in the scenario of turbulence regulated star formation (e.g., Elmegreen & Scalo 2004; Krumholz & McKee 2005).

To gauge the effect of the mass distribution on the star formation rate, we plot in Fig. 6(b) the SFR in the limit that all mass above a given density ρ is converted into stars in one free fall time at the average density of that mass. The limiting rate is normalized by

the global free-fall rate defined in equation (1), which in our simulation has a value of

$$\dot{M}_{\text{ff}} = 4.32 \times 10^2 \frac{c_s^3}{G}, \quad (11)$$

much larger than the classical value of $0.975c_s^3/G$ for the inside-out collapse of a singular isothermal sphere (Shu 1977). The distribution of the free-fall rate has a broad peak around $0.4 \rho_0$. At lower densities, it increases with density, as a result of mass clumping into moderately overdense regions which, by itself, worsens the problem of rapid star formation. At densities above the peak, the mass fraction drops off with density faster than inverse square root of the density, leading to a decline of the free fall rate. For comparison, we note that the actual rate of star formation in the simulation is $\sim 0.03\dot{M}_{\text{ff}}$, or $\dot{M}_* \approx 13 c_s^3/G$.

We next consider the distribution of the column density, which is more accessible to direct measurement than the volume density. In Fig. 7, we plot the column density PDFs at the representative time along the three axes. The PDFs along the y - and z -axes are broader than that along the x -axis. The broader distributions are caused by mass settling along the field lines; when viewed perpendicular to the field lines, the column density is enhanced in the plane of mass concentration and decreased away from it. The PDFs deviate significantly from lognormal distributions, especially towards the high density end. The deviation is larger than those found by, for example, Ostriker et al. (2001) for decaying turbulence. One difference is that our turbulence is driven, indeed in a specific way—by collimated outflows. Perhaps more importantly, our prescription of star formation enables us to run the simulation longer, which allows more time for the cloud material to condense gravitationally into cores and filaments. In addition, the global gravitational potential well is deeper in our simulation. The cluster-wide gravity tends to concentrate dense cores and filaments towards the bottom of the potential well, increasing their chance for overlap, especially when viewed along the plane of mass concentration perpendicular to the large scale magnetic field. The overlap skews the PDF towards the high column density end.

To examine the spatial distribution of the mass more quantitatively, we plot in Fig. 8 the average density as a function of radius at the representative time. The averaging is done in concentric shells centered on the location of minimum gravitational potential. We exclude in the log-log plot the central part of the cloud where the number of grid cells is small and the shell radius is ill-defined. There is a clear trend for the averaged density outside the central (excluded) region to drop off with radius, in an approximately power-law fashion. A similar drop-off is found at the two other times (1.0 and 2.0 t_g) shown in Fig. 8. A power-law $\rho \propto r^{-1.5}$ is also plotted for comparison. Although the power-law provides a fair (although not unique) description of the averaged density distribution, it should be kept in mind that the medium is very clumpy. The clumpiness is illustrated vividly in Fig. 4, where the volume density on a representative slice through the computational domain is displayed.

3.5. Velocity Power Spectrum

The power spectrum of a turbulence in the inertial range (between the energy input and dissipation scales) can often be approximated by a power law, $E_k = k^2 v_k^2 \propto k^{-n}$, where k is the wavenumber. The power index n holds clues to the nature of the turbulence. For example, the incompressible Kolmogorov turbulence has $n = 5/3$. For the shock-dominated Burgers turbulence, the index is $n = 2$. Some simulations of driven turbulence obtained a power index $n \approx 1.74$ for isothermal gas (Boldyrev et al. 2002), which is closer to the Kolmogorov than Burgers value. The exact value of the power index depends, however, on model parameters, particularly the degree of cloud magnetization (Vestuto et al. 2003). In our standard simulation, the power spectra deviate strongly from a single power-law. The deviation is illustrated in Fig. 9, where the spectra at three times (1.0, 1.5 and 2.0 t_g) are plotted. They all appear to have a break around $k_b \approx 0.6$ ($2\pi/L_J$). Below k_b , the spectra are rather flat. They steepen to approximately $k^{-2.5}$ above the break. The shape of the spectra indicates that the bulk of the power resides near the break rather than at the smallest wavenumber.

The break k_b in the power spectrum corresponds to a characteristic length scale $L_b = 2\pi k_b^{-1} \approx 1.7L_J$, which is about 1/5 of the size of the simulation box. The scale L_b can plausibly be identified with the typical outflow length L_f . A crude estimate of L_f comes from the distance that the (conical) jet component of the outflow travels before it is slowed down to the ambient turbulent speed ($v_{\text{turb}} \approx 5c_s$). Assuming a constant ambient density at the average value ($0.15\rho_0$), we obtain $L_f \approx 2.8L_J$, which is about 65% larger than L_b . However, the stars are formed preferentially in dense regions near the bottom of the potential well. The higher-than-average ambient density should lower the estimated outflow length somewhat, bringing it to a closer agreement with the characteristic break length. The outflow may be further shortened by magnetic tension if it propagates perpendicular to the large scale magnetic field. These considerations lead us to believe that the break in the power spectrum is produced by the momentum injection from protostellar outflows, although the strong inhomogeneity in the mass distribution makes it difficult to predict the length of any individual outflow accurately. Some outflows may be trapped close to where they are produced, while others may cross the entire cloud through largely empty regions. Matzner (2007) independently argued for the existence of a break in the power spectrum using a similar reasoning.

Breaks are also seen in the power spectra of the turbulence driven in Fourier space. For example, Vestuto et al. (2003) drove their turbulence with a power peaking at a scale that is 1/8 of the box size. They found a break near the driving wavenumber. In the inertia range above the break, they found that the power index n decreases with increasing magnetic field

strength. Our standard simulation has a field strength comparable to their model B, which has an estimated power index $n = 2.0$. This index is smaller than that in our simulation. A potential cause for the difference is that their model B has a resolution higher than ours by a factor of 2, and Vestuto et al. have shown that a higher resolution tends to yield a smaller index. However, our preliminary analysis of a higher resolution (256^3) simulation indicates that in the inertial range the power index is essentially the same as that of our current simulation. The difference may instead result from the fact that self-gravity is included in our simulations but not in theirs and, perhaps more importantly, that our turbulence is driven by discrete, highly anisotropic outflows rather than isotropically in Fourier space. Anisotropy due to the collimation of individual outflows and the correlation of outflow directions is an important feature that distinguishes our turbulence simulations from the others and this feature is usually not taken into account in Kolmogorov-type dimensional analyses; the effects of anisotropic driving remain to be fully explored. The difference in turbulence driving is also reflected in the flattening of our power spectra at the highest wavenumbers (see Fig. 9). The flattening is most likely produced by the spherical component of the outflow, which supplies energy on small scales.

The relatively flat power spectrum at small wavenumbers below the break k_b is more interesting. Some of the power may come from inverse cascade. However, the inverse cascade in the simulations of Vestuto et al. (2003) produced an E_k below the break wavenumber that decreases quickly towards small k roughly as $E_k \propto k^2$. In contrast, the E_k in our simulation generally remains flat or continues to increase slowly towards small k . We believe that most of the power below the break k_b is supplied directly by collimated outflows rather than through inverse cascade. Movies of the standard simulation show clearly that many outflows can break out from the dense cores surrounding their driving sources and propagate to large distances, sometimes across the entire simulation box, injecting energy and momentum on the largest possible scale. Since the outflow propagation is well resolved in our simulations, we believe that the general conclusion that the power spectrum E_k flattens at small wavenumbers is robust, although the details may depend on the outflow treatment and may be affected by the periodic boundary condition.

The power spectrum of the protostellar turbulence can be decomposed into a solenoidal and compressible component. We find that the solenoidal component always dominates the compressible component. This is in qualitative agreement with previous simulations. Quantitatively, the solenoidal component is larger by a factor of ~ 10 at wavenumbers above the break k_b . Below the break, the factor is somewhat lower. Overall, the ratio of the two components is comparable to those found by Boldyrev et al. (2002) and Vestuto et al. (2003), who drove their turbulence by a purely solenoidal velocity field. The similarity indicates that the driving of protostellar turbulence by collimated outflows is probably mostly solenoidal,

as one may expect from the large velocity shear between the fast outflow and the ambient medium.

3.6. Stellar Component

The simple prescription adopted in our model for star formation makes detailed comparison between the predicted stellar properties and observations premature at this stage of model development. Nevertheless, there are a few general features of the model stars that are worth noting. These include the spatial distribution of the stars relative to the gas, and their velocity dispersion.

We illustrate the stellar distribution in Fig. 10, where the positions of the 80 stars at the representative time $1.5 t_g$ are projected onto the x - y plane. Also plotted in the figure are contours of the column density along the z -axis, which delineate the gas distribution. The densest regions appear to form an “S-shaped” ridge. The elongation is caused mainly by mass settling along the large-scale magnetic field lines, which run more or less horizontally in the plot. There are two separate concentrations of dense gas, with the main one near the center of the column density map, and the secondary one to the lower right. The majority of stars are clustered around the main gas concentration. Specifically, slightly more than half of all stars (41 out of 80) are located within a radius $0.75 L_J$ (or 0.125 pc for the fiducial parameters) of the center. In this localized region, the SFE is 15.7%, much higher than that of the clump as a whole (4.2%). The less massive concentration of dense gas is forming a smaller group of stars.

The degree of stellar clustering is expected to depend on age. To show the age dependence, we divide the stars into two groups: those born before and after $1 t_g$. They have 34 and 46 members respectively. The two groups of stars are represented by two different symbols and colors in Fig. 10. It is clear that the younger stars are more closely associated with the dense gas at the current time and the older stars are more spread out, as expected. Part of the reason for the older stars to be more widely dispersed is that they have had more time to spread out. Another part is that the older stars are bound less tightly to the cluster-forming region as a whole. Indeed, 12 of the 34 older stars (or 35%) have positive total (kinetic minus gravitational) energies, and are thus formally unbound to the cluster at the time under consideration. The unbound fraction goes down to 8.7% (or 4 out of 46) for the younger stars. The difference in the unbound fraction comes primarily from the tendency for the older stars to locate higher up in the potential well. As a result, they are able to move around more freely. If the gas in the cluster-forming region that gravitationally binds the majority of the stars together were to be removed suddenly, the stellar cluster would

dissolve quickly.

An important quantity that can in principle be directly measurable is the velocity dispersion of the stars. In Fig. 11, we plot the velocity dispersion σ_* , defined as the rms value of the stellar velocities relative to the mean⁴, as a function of time for the standard model. Except for a brief initial period (when the number of stars is still small), the dispersion σ_* ranges from ~ 4 to $\sim 6 c_s$. It is comparable to the mass-weighted average turbulent speed v_{turb} of the gas, which is also shown in the figure for comparison. Even though σ_* and v_{turb} are defined somewhat differently, the fact that they are comparable is significant: both speeds reflect the depth of the global gravitational potential well. In particular, there is a significant increase in both σ_* and v_{turb} starting around $1 t_g$. Their increase appears to track the increase in the absolute value of the gravitational energy around the same time (see Fig. 3).

Before leaving the section on the standard model, we comment briefly on the dense cores, a number of which show up prominently in Fig. 10 (see also Fig. 4). These cores are the “crown jewels” of the protostellar turbulence—the basic units of individual star formation. They tend to cluster near the bottom of the potential well. Whether they are created mostly in-situ near the bottom is unclear; some of them could be produced higher up in the potential well and later “sink” to the bottom. In any case, the spatial concentration of dense cores increases the chance for core-core interaction, particularly coalescence, which can build up the core mass. One the other hand, the mass of a core may be limited by gravitational collapse and disruption through outflows associated with star formation. The resulting core mass spectrum may hold the key to the determination of IMF (Motte et al. 1998). We will postpone a detailed investigation of these core-related topics (including the role of outflow triggering) to future, higher resolution studies.

4. Variations on the Standard Model

4.1. Spherical versus Collimated Outflows

Protostellar outflows are collimated, particularly during the earliest, Class 0 phase of (low-mass) star formation. It is during this phase that the bulk of the mass of a star is

⁴In computing σ_* , we exclude the two stars that move at speeds of 81.6 and $135 c_s$, respectively, much faster than the other stars. Such fast moving stars are produced, on rare occasions, when the density in a fast moving outflow is pushed above the threshold for mass extraction. They may disappear with a refined outflow treatment.

assembled. If the outflows are driven by the gravitational energy release associated with mass accretion, then the bulk of their energy and momentum is expected to be injected into the ambient medium during this phase. This expectation is consistent with the observations of Bontemps et al. (1996), which showed that molecular outflows—the ambient material set into motion by the outflow-ambient interaction—are most powerful for the Class 0 sources; they tend to become weaker and broader with time (Bachiller & Tafalla 1999). It is the momentum carried in the powerful molecular outflows in the early stages of star formation that we seek to capture with our outflow prescription (see the Appendix); the optical jets observed at later times (Bally & Reipurth 2001) and possibly the more tenuous wide-angle winds that are predicted to surround the jets in the magnetocentrifugal wind theory (Shu et al. 1995) are not included explicitly in our current model; their inclusion would only make the feedback from star formation stronger.

We illustrate the effects of outflow collimation using three variants of the standard model. These variants include a spherical model that does not have a jet component at all (Model E1 in Table 1), and two models with weaker jet components (Model E2 with a jet momentum fraction $\eta = 0.25$, and Model E3 with $\eta = 0.50$). Other quantities, including the dimensionless parameter f for outflow strength, are kept the same as in the standard model. In Fig. 12, we plot the time evolution of the SFE for all four models. The SFEs remain relatively close together until about $1.0 t_g$. Between 1.0 and $2.0 t_g$, there is a clear trend that the SFE decreases as the strength of the jet component increases relative to the spherical component. In particular, the SFE increases from ~ 0.02 to ~ 0.20 in the spherical model and to only ~ 0.06 in the standard jet model. The difference between the two in the total mass of the stars formed during this time interval is a factor of ~ 4.5 . We conclude that collimated outflows are more efficient in suppressing star formation in the protostellar turbulence than the spherical outflow carrying the same amount of momentum.

The above difference in SFE can be understood in terms of where the outflow momentum is deposited. Collimated outflows can propagate well outside the dense regions near the bottom of the potential well, where most stars form. They deposit a large fraction of their momenta in the outer envelope, where most mass resides. Spherical outflows, on the other hand, are more easily trapped. They tend to drive turbulent motions on a smaller scale, which are dissipated more quickly. The higher rate of turbulence dissipation in the spherical outflow model is compensated by a faster turbulence replenishment, through a higher rate of star formation. To fuel the higher star formation rate, more material must be concentrated into dense regions that can collapse to form stars. The mass concentration is reflected in the PDFs of the volume and column densities, both of which tend to be strongly skewed towards the high value end compared with lognormal distributions. The column density PDF is particularly noteworthy. In addition to a main peak similar to that shown in Fig. 7

for the standard jet case, it often displays a broad shoulder or even a second peak to the right of the main peak, as illustrated in Fig. 13. Such strong deviations from a lognormal distribution may be detectable in regions of active cluster formation when the outflows are trapped relatively close to their driving sources.

4.2. Effects of Outflow Strength

The exact value of the outflow parameter f is uncertain. In the Appendix, we have estimated a plausible range of $P_* = 10 - 100$ km/s for the outflow momentum per solar mass of stellar material, corresponding to $f = 0.1 - 1$. To illustrate the effects of outflow strength, we have rerun the standard simulation but with a lower ($f = 0.25$, Model F1) and higher ($f = 0.75$, Model F2) outflow strength. The SFEs of these simulations are plotted in the upper panel of Fig. 14. There is a clear trend for the SFE to increase with decreasing outflow strength. Indeed, the SFE is nearly inversely proportional to the outflow strength parameter f , so that their product is roughly the same for all three cases, as shown in the lower panel of the figure. Apparently, the total amount of momentum injected into the cloud is insensitive to the strength of individual outflow: the reduction in the momentum supplied per outflow is more or less compensated by the increase in the number of stars (and thus outflows). In contrast, the total amount of kinetic energy injected increases roughly linearly with the outflow strength. The difference is consistent with the expectation that the momentum of protostellar outflow is more directly relevant for turbulence replenishment than the energy; the latter dissipates more readily.

Model F1 with $f = 0.25$ is particularly interesting. It demonstrates that even relatively weak outflows are capable of driving a robust protostellar turbulence in which the SFR is reduced well below the limiting free-fall rate. In the reminder of the subsection, we will discuss this model in some detail, and contrast it with the standard model, starting with the energy evolution. As shown in Fig. 15, the total kinetic energy drops quickly, before being pumped up by the outflows associated with the (bursty) star formation. Compared with the standard model, the kinetic energy here is more comparable with the gravitational energy, because it is less dominated by the (weaker) active outflows. The absolute value of the gravitational energy is somewhat higher than that in the standard model, indicating that the bulk of the cloud material is more tightly bound. It increases initially, as a result of gravitational settling of the mass in the cluster-forming region towards the bottom of the potential well due to turbulence dissipation. The increase is stopped around $1 t_g$ when enough motions are generated by outflows to arrest further contraction. There is some undulation at later times, which is also evident in the standard model (see Fig. 3). The existence of

such mild oscillations in the gravitational energy may not be too surprising, given the bursty nature of the star formation. The amplitude of the oscillation is small, again indicating that the cluster-forming system is hovering close to an equilibrium.

We have examined the quasi-equilibrium state of the weaker outflow model at the representative time $1.5 t_g$, and found it similar to that of the standard model discussed in § 3. In particular, the turbulent velocity field contains many distinct patches of more or less coherent motions. The average infall and outflow speeds are -1.86 and $2.57 c_s$, respectively. The net average radial speed is only $1.09 \times 10^{-2} c_s$, much smaller than the average infall and outflow speeds and the sound speed. The infall and outflow momenta nearly balance each other, with the slower infall speed compensated by a larger amount of infalling mass, as in the standard model. The mass weighted PDF of the volume density can again be fitted reasonably well with a lognormal distribution. The PDFs of the column density deviate more strongly from lognormal, especially along directions perpendicular to the initial magnetic field direction. A prominent break is present in the velocity power spectrum, as in the standard case. The similarities lead us to conclude that the gross properties of the protostellar turbulence are insensitive to the outflow strength.

4.3. Effects of Magnetic Field

We illustrate the effects of the magnetic field using three models of different field strengths. They are Models M1, M2, and S0 in Table 1, specified by $\alpha = 10^{-6}$, 0.5 and 2.5, respectively. For the standard model ($\alpha = 2.5$), the dimensionless mass-to-flux ratio $\bar{\Gamma} = 0.52$ for the clump as a whole, as mentioned earlier. This ratio drops to 0.23 and 3.3×10^{-4} for $\alpha = 0.5$ and 10^{-6} . In all three cases, the ratio is substantially less than unity, indicating that the global magnetic field is not strong enough to suppress star formation altogether. Stars are indeed formed in all three cases, as shown in Fig. 16, where the SFEs of the models are plotted. There is a clear trend for the SFE to decrease with increasing field strength, as one might expect. Specifically, the magnetic field in the standard model ($\alpha = 2.5$) has reduced the rate of star formation by a factor of ~ 2.2 compared to the negligible field case ($\alpha = 10^{-6}$). Even the relatively weak field in the $\alpha = 0.5$ model appears to have a significant effect on the rate of star formation, reducing it by a factor of ~ 1.6 .

A simple, albeit crude, way to gauge the dynamical importance of a magnetic field is to compare its energy to the kinetic energy of the gas. In our case, the comparison is complicated by the fact that the kinetic energy is often dominated by active outflows. For example, in the standard simulation with $\alpha = 2.5$, 81% of the energy is carried by 8.6% of the mass that moves faster than $10 c_s$ at the representative time $1.5 t_g$. The remaining

energy is carried by the bulk, more slowly moving material. It has a value of 8.80×10^2 in units of $\rho_0 c_s^2 L_J^3$, corresponding to a mass-weighted rms speed of $4.55 c_s$, comparable to the specific (scalar) momentum (see Fig. 2). This portion of kinetic energy is smaller than the total magnetic energy at the same time ($2.63 \times 10^3 \rho_0 c_s^2 L_J^3$). However, the magnetic energy is dominated by the background uniform field, which accounts for $1.82 \times 10^3 \rho_0 c_s^2 L_J^3$. The remaining $8.06 \times 10^2 \rho_0 c_s^2 L_J^3$, carried by the distorted magnetic field, is remarkably close to the kinetic energy carried by the bulk of the turbulent material away from the active outflows ($8.80 \times 10^2 \rho_0 c_s^2 L_J^3$). The similarity indicates that an energy equipartition is reached between the distorted magnetic field and the turbulent motions of the bulk material for the standard model, which has a moderately strong magnetic field to begin with.

The weaker field case of $\alpha = 0.5$ (Model M2) is more intriguing. At the beginning of the simulation, the magnetic energy is only $3.65 \times 10^2 \rho_0 c_s^2 L_J^3$, well below the kinetic energy. By the representative time $1.5 t_g$, it has nearly quadrupled to $1.38 \times 10^3 \rho_0 c_s^2 L_J^3$. Most of this energy is stored in the distorted magnetic field, which accounts for $1.02 \times 10^3 \rho_0 c_s^2 L_J^3$. The distorted field energy is higher than its counterpart in the standard model by 27%, despite the fact that the standard model is more strongly magnetized to begin with. This energy is again close to the kinetic energy carried by the bulk of the cloud material that moves at a speed below $10 c_s$ ($1.11 \times 10^3 \rho_0 c_s^2 L_J^3$). Apparently, the magnetic energy has been amplified to an equipartition level in this initially weaker field case. Part of the amplification comes from the concentration of mass towards the bottom of the potential well, which drags the field lines into pinched configurations. The pinched field lines are evident in Fig. 17, which shows the field structure and isodensity surfaces in 3D. More dramatic amplification comes from the stretching of field lines by fast moving outflows, which creates large magnetic distortions that are relatively long lived. Further amplification comes from the turbulent motions of the (slower) bulk material. These processes remain to be quantified.

The amplification factor is even larger for the weakest field model of $\alpha = 10^{-6}$. The initial magnetic energy is $7.29 \times 10^{-4} \rho_0 c_s^2 L_J^3$. It increases to $0.46 \rho_0 c_s^2 L_J^3$ at $1.5 t_g$, by a factor of 630. Despite the large enhancement factor, the magnetic energy is still orders of magnitude below the kinetic energy, indicating that the magnetic field is dynamically unimportant in this extreme case. We conclude that magnetic fields are dynamically important in protostellar turbulence as long as their strengths are not much below the critical value to begin with. The role of magnetic fields is discussed further towards the end of § 5.1 below.

5. Discussion

5.1. The Nature of Protostellar Turbulence

A salient feature of protostellar turbulence is the simultaneous existence of infall and outflow motions. Fluid parcels are pushed up the gravitational potential well by outflows. Once slowed down, they are pulled back towards the bottom of the potential well by gravity, setting up a vigorous circulation of material between the dense central region where most stars form and the outer envelope, where most of the mass resides. The circulation is in a way reminiscent of convection, although the fluid motions are highly supersonic, unlike the conventional buoyancy-driven convection. In this picture, the gravity plays a role as important as the outflows. It drives infall motions that close the global circulation, enabling the system to reach a quasi-equilibrium state, in which the infall and outflow motions are globally balanced. Simultaneous infall and outflow are observed in a number of embedded clusters, including NGC 1333 (Walsh et al. 2006; Knee & Sandell 2000), the Serpens cloud core (Williams & Myers 2000; Olmi & Testi 2002; Davis et al. 1999), and NGC 2264 (Peretto et al. 2006; Williams & Garland 2002; Wolf-Chase et al. 2003). Such observations underpin our notion of cluster formation in outflow-driven protostellar turbulence.

There are several lines of evidence for a quasi-equilibrium state in all of our simulations. First, the global infall and outflow momenta nearly cancel, yielding a net mass-weighted velocity in the radial direction much smaller than the average infall or outflow velocity overall. There are, however, regions where one dominates the other and the equilibrium is locally upset. Second, both the specific momentum and gravitational energy approach, and oscillate with a small amplitude around, a constant value at late times, indicating that an equilibrium has been reached. The total kinetic energy is not as good an indicator of equilibrium, since it is typically dominated by fast moving transients. The kinetic energy for the regions away from active outflows is, however, comparable to the gravitational energy, suggesting a rough virial equilibrium for the bulk material. In addition, the spherically averaged density distribution as a function of radius appears to settle into a power-law of roughly constant power index in the envelope. The density PDFs and velocity power spectra also maintain similar shapes at late times. All these lines of evidence point to the existence of a quasi-equilibrium state with fully developed protostellar turbulence; it is in such an environment that the majority of the cluster members form.

Stars form at a relatively slow rate. In our standard model, only $\sim 3\%$ of the gas is converted into stars per free fall time at the average density. This corresponds to a remarkably long gas depletion time of ~ 33 free fall times. The exact value of the star formation rate depends on several factors, including the strength and degree of collimation

of the outflow, as well as the initial magnetic field strength (and perhaps topology, which is not explored here). Although there is considerable uncertainty in estimating each of these factors, we believe that the general conclusion that outflows can maintain the turbulence in a cluster forming clump is robust. At a fundamental level, there is enough momentum in the outflows to replenish the momentum dissipated in the turbulence for a reasonable star formation efficiency of order 10%, as stressed by McKee (1989) and Shu et al. (1999), among others, as long as the momentum dissipation time is not much shorter than the free fall time. Our detailed simulations allowed us to estimate the dissipation time self-consistently. For the set of models with relatively strongly magnetic fields ($\alpha = 2.5$) and collimated outflows (Models S0, M1 and M2), the average dissipation time, as measured by the ratio of the equilibrium (scalar) momentum and the rate of momentum input, is close to the free-fall time \bar{t}_{ff} at the average density, more or less independent of the outflow strength. The dissipation time increases with the strength of the magnetic field and the degree of outflow collimation.

The velocity field of protostellar turbulence is dominated by the solenoidal (or shear) component. Such a velocity field is perhaps to be expected, given that there is a large shear between the collimated outflows and the ambient medium, and that any fast compressive motions that may have also been generated by the interaction are readily dissipated in shocks. Indeed, the large ratios of the kinetic energies in the solenoidal and compressive components obtained in our simulations are similar to those obtained in Boldyrev et al. (2002) and Vestuto et al. (2003), where the turbulence is driven isotropically in Fourier space using a purely solenoidal velocity field. Our protostellar turbulence is a special case of driven turbulence: it is driven by discrete, fast-moving, collimated outflows (see also Mac Low 2000), that come from the protostars formed preferentially near the bottom of the potential well. For turbulence driven in Fourier space, the dissipation rate depends on the scale of driving (e.g., Mac Low 1999), with those driven on small scales decaying faster than those driven on large scales. A well recognized problem with driving in Fourier space is that it affects the gas in the entire computation box simultaneously (e.g., Elmegreen & Scalo 2004). The more physical outflow-driving acts sequentially on a range of scales, from near the protostars to large distances, and anisotropically, both on the local scale of individual star formation and on the global scale of cluster-forming clump; the latter comes about because the outflow orientations are not completely random in the presence of a strong magnetic field. The amounts of energy and momentum deposited on different scales depend on both the intrinsic properties of the outflows (such as the flow speed, degree of collimation, duration, etc), and the (generally anisotropic) distributions of mass and magnetic field in both the dense cores that surround the outflow-driving protostars and the general turbulent background. Despite these differences, our finding that the turbulence driven by collimated

outflows decays more slowly than that driven by spherical outflows is qualitatively consistent with the previous result, since collimation effectively increases the scale of driving.

Magnetic fields can influence the protostellar turbulence in several ways. If strong enough, they can flatten the mass distribution and affect, perhaps even control, the directions of outflow ejection and propagation. In our simulations, we find that the energy stored in the distorted magnetic field is comparable to the kinetic energy of the bulk cloud material away from active outflows, as long as the field strength is not far below the critical value to begin with; relatively weak fields are amplified by gas motions to an equipartition value. An implication is that the turbulent motions for the bulk of the gas is roughly Alfvénic, and the magnetic field is dynamically important. Indeed, the field may be crucial in transmitting the outflow energy and momentum to regions not directly impacted by outflows, through large amplitude Alfvén waves. It may also prevent dense fragments from moving freely in the clump potential, since they need to drag along the ambient material linked to them through magnetic field lines (Elmegreen 2006). These effects remain to be fully quantified.

Approximate equipartition between the magnetic and turbulent kinetic energies is inferred in regions with Zeeman measurements of the magnetic field strength (e.g., Myers & Goodman 1988; Crutcher 1999). For the energy in the measured (ordered) magnetic field to be comparable to the turbulent kinetic energy, the flux-to-mass ratio probably needs to lie within a factor of a few of the critical value (as in the standard simulation). Such a ratio may be obtained naturally if the cluster-forming clumps are created quickly out of a more diffuse, magnetically subcritical medium through strong shocks, driven perhaps by HII regions or supernova explosions. The strong C-shock may reduce the flux-to-mass ratio in the shocked layer below the critical value, inducing a relatively rapid subsequent evolution (collapse and star formation) that freezes the flux-to-mass ratio at a value somewhat below the critical value. In this picture of externally triggered clump formation out of a (perhaps moderately) magnetically subcritical cloud (to be quantified elsewhere), the magnetic energy would be automatically comparable to the turbulent kinetic energy, and be a significant factor in regulating star formation in clusters.

To summarize, the protostellar turbulence in active regions of cluster formation is outflow-driven, gravity-assisted, and magnetically mediated.

5.2. Connection to Previous Work and Observations

The present investigation is a first step towards a quantitative theory of cluster formation in outflow-driven protostellar turbulence. Our emphasis has been on the global

properties of the turbulence. Supersonic turbulence in molecular clouds has been subject to intensive numerical studies in recent years (as reviewed, e.g., by Elmegreen & Scalo 2004). A longstanding problem is that it decays away quickly, which prompted many workers to drive the turbulence in Fourier space. The most important distinction of our simulations is that we drive the turbulence in physical space, using outflows that are ubiquitously observed in star formation.

There have been a few previous studies of turbulent motions driven by outflows. Allen & Shu (2000) examined the effects of outflows on the dynamics of critically magnetized, sheet-like GMCs. The same 2D geometry is adopted in our previous investigation of star formation in turbulent, magnetically subcritical clouds that includes both ambipolar diffusion and outflows (Nakamura & Li 2005). These 2D calculations are extended in this paper to three dimensions (but without ambipolar diffusion). The only other 3D study is that of Mac Low (2000). He conducted a preliminary investigation of continuous driving of turbulence in a non-self-gravitating cloud by outflows ejected from a number of randomly distributed locations that are fixed in space and time. We went beyond this study by including self-gravity and connecting the outflows to the discrete events of star formation, which occur preferentially near the bottom of the potential well.

The protostellar outflow has a unique feature that can be potentially observable. It has a velocity power spectrum characterized by a prominent break. At small wavenumbers, the spectrum remains relatively flat. It steepens to approximately $E_k \propto k^{-2.5}$ above the break. The broken power-law spectrum implies that the bulk of the energy resides near the break, rather than at the smallest wavenumber. Given that the turbulence is driven by a collection of outflows of varying lengths, there is no prior reason why the power should be dominated by the largest scale of the system. In particular, the Larson's (1981) linewidth-size relation is unlikely to be strictly applicable *inside* parsec-scale clumps of active star formation, as recognized independently by Matzner (2007). High resolution observations of nearby embedded clusters that resolve the gas kinematics on different scales can be used to test this proposition (e.g., Caselli & Myers 1995; Saito et al. 2006).

Another way to probe the nature of the turbulence is through probability distribution functions (PDFs). Although the PDFs of the volume density in protostellar turbulence can often, but not always, be fitted reasonably well by lognormal distributions, the PDFs of the column density show considerable deviations, especially towards the high value end and in regions of rapid star formation. The strong deviation is not necessarily a unique signature of the protostellar turbulence per se. More likely, it is a reflection of the crucial role that the gravity plays in our simulations. The gravity allows dense cores to form and collapse individually, and to cluster near the bottom of the potential well collectively. The

ability to follow the cloud evolution to a later stage of gravitational evolution distinguishes our simulations from other grid-based simulations of cluster formation in turbulent clouds (e.g., Heitsch et al. 2001; Ostriker et al. 2001; Li et al. 2004; Tilley & Pudritz 2004; Vazquez-Semadeni et al. 2005; for examples of SPH simulation of cluster formation, see Klessen et al. 1998 and Bate et al. 2003). Such simulations are typically terminated before the runaway collapse of the densest core, before the primordial turbulence is transformed into a protostellar turbulence through the outflows associated with star formation. We are able to go well beyond the collapse of the first core and follow the formation of multiple generations of stars and their feedback into the cluster-forming environment, albeit using simple prescriptions for the subgrid physics. We hope to refine these prescriptions in the future.

5.3. Limitations and Future Refinements

The most restrictive prescription is perhaps the mass of individual stars. We have on purpose kept the stellar mass close to a single value, about $0.5 M_{\odot}$ for the fiducial choices of parameters, which is comparable to the typical mass of low mass stars. The prescription, however, decoupled the properties of the dense cores and the stars that they produce. This is obviously an oversimplification. A better prescription is perhaps to assume a constant accretion time for all stars. Some motivation for this prescription comes from the analysis of Myers & Fuller (1993), who inferred a spread in mass accretion time for stars between 0.3 and $30 M_{\odot}$ much smaller than the spread in stellar mass. Ultimately, high resolution calculations, using perhaps adaptive mesh refinement (AMR), are required to follow the process of mass accretion in detail to determine the stellar mass self-consistently. Even with AMR, there are uncertainties of physical origin that cannot be eliminated with higher resolution: the effects of jets and winds from young stellar objects (as well as radiation for massive stars), which can interfere with the process of mass accretion and limit the stellar mass (Nakano et al. 1995; Matzner & McKee 2000; Shu et al. 2004).

In our simulation, the momentum of the primary outflow from close to a star is assumed to be imparted instantaneously to a small region immediately next to the star. While we believe that this simple prescription captures the essence of the outflow feedback, a more realistic treatment would be to include the primary protostellar wind in the simulation for a finite duration. A potential difficulty with such a treatment is that the high wind speed may reduce the time step to the point of making the global simulation prohibitive. Another possibility is to carry out separate calculations of core collapse and outflow propagation (e.g., Shang et al. 2006), and find general rules that can be used in the global calculations.

In any case, a detailed treatment of outflow-ambient interaction is needed for not only the determination of the mass of an individual star in a given core, but also the outflow-shaped environment for the cluster formation. The theoretical treatment can benefit greatly from systematic observations that quantify the dependence of outflow properties on the stellar mass and star-forming environments, if any. There is a pressing need for such observations.

Another area of future improvement will be in spatial resolution. Higher resolution is desirable for at least two reasons. First, the protostellar turbulence appears to be dominated by shearing rather than compressible motions. The shear may excite small scale turbulence that may be washed out by numerical diffusion on a relatively coarse grid, although the magnetic field may suppress the development of such a turbulence. More importantly, higher resolution will allow us to study the properties of dense cores with greater confidence. Dense cores in some cluster forming regions appear to have mass spectra similar to the IMF. Understanding this important observation will be a focus of our future higher resolution simulations.

Lastly, we reiterate that the standard periodic boundary condition is adopted in our simulations. It has the undesirable effect of preventing energy and momentum, carried by either outflowing material or MHD waves, from leaving the simulated region. This effect may be compensated to some extent by the energy and momentum fed into the region from the ambient environment. A consequence of this restriction is that we are unable to follow cloud disruption by outflows, which may terminate the formation of relatively poor clusters that do not contain massive stars.

6. Summary

We have carried out numerical simulations of cluster formation in protostellar outflow-driven turbulence. Our emphasis was on the global properties of the gas and the star formation rate. The main results are summarized below.

1. Protostellar outflows of strength in the observationally inferred range can readily replenish the supersonic turbulence in clumps of active cluster formation against dissipation, and keep the clumps close to a dynamical equilibrium. The protostellar turbulence is characterized by the coexistence of infall driven by gravity and outflow motions. These motions are roughly balanced so as to yield a net mass flux towards the bottom of the gravitational potential well much smaller than that expected in a global free-fall collapse.
2. The protostellar turbulence is maintained by outflows associated with star formation at rates as low as a few percent per free fall time. Collimated outflows are more efficient in

driving the turbulence than spherical outflows carrying the same amount of momentum. Collimation enables an outflow to propagate farther away from its source, effectively increasing the scale for energy and momentum injection. This result is in agreement with the previous finding that turbulence driven on a larger scale decays more slowly. Although protostellar outflows tend to retard global star formation, they can directly trigger star formation in localized regions through shock compression.

3. There is a prominent break in the velocity power spectrum of the protostellar turbulence. Below the break wavenumber, the spectrum is relatively flat. It steepens at higher wavenumbers. The break may provide a handle to distinguish the outflow-driven protostellar turbulence from other types of turbulence. In particular, it is unlikely that the Larson’s linewidth-size holds on the scales of relatively flat power spectrum. Another general feature is that the turbulent velocity field is dominated by the solenoidal component, produced perhaps by the strong shear between the outflow and the ambient medium. The high degree of anisotropy in the turbulence driving is an important feature of the protostellar turbulence that warrants further investigation.

4. We find that the PDFs of the volume density in the cluster-forming clump can be approximated reasonably well by lognormal distributions in general. The PDFs of the column density, on the other hand, often show large deviations from lognormal, especially when the ordered magnetic field is strong enough to flatten the mass distribution along the field lines, and in regions of rapid star formation. Dense cores and filaments, which cluster near the bottom of the potential well, tend to skew the column density PDFs towards the high value end. The mass distribution in the cluster forming region is very clumpy. Nevertheless, the spherically averaged density typically increases with decreasing radius in an approximately power-law fashion in the envelope, with $\rho \propto r^{-1.5}$ providing a reasonable fit to the profile in many cases.

5. Magnetic fields are dynamically important for cluster formation even in magnetically supercritical clumps, as long as the initial field strength is not much below the critical value to begin with. Moderately strong fields can significantly reduce the rate of star formation. Even a relatively weak magnetic field can be amplified to an equipartition level by the outflow-driven turbulent motions. The magnetic field is expected to influence the directions of outflow ejection and propagation and the transmission of outflow energy and momentum to the ambient medium, although these effects remain to be fully quantified.

6. We find that the stellar velocity dispersion is comparable to the turbulent speed of the gas. More detailed predictions on the stellar properties await a refined treatment of the subgrid physics of individual star formation.

This work is supported in part by a Grant-in-Aid for Scientific Research of Japan (1540117), a Grant for Promotion of Niigata University Research Projects, and NSF and NASA grants (AST-0307368 and NAG5-12102). We thank Chris Matzner for sharing some results prior to publication and the referee for comments that improved the presentation of the paper. The numerical calculations were carried out mainly on SX6 at Niigata University, on SX8 at YITP in Kyoto University, and on SR8000 at Center for Computational Science in University of Tsukuba.

REFERENCES

Allen, A. & Shu, F. H. 2000, *ApJ*, 536, 368

Allen, L. E., Megeath, T., Gutermuth, G., Myers, P. C., et al. 2006, in *Protostars and Planets V*, eds. B. Reipurth, D. Jewitt & K. Keil (Univ Arizona Press), in press

Anderson, J. M., Li, Z.-Y., Krasnopolksy, R., & Blandford, R. D. 2005, *ApJ*, 630, 945

Aspin, C. 2003, *AJ*, 125, 1480

Bachiller, R., Perez Gutierrez, M., Kumar, M. S. N. & Tafalla, M. 2001, *AA*, 372, 899

Bachiller, R. & Tafalla, M. 1999, in *The Origins of Stars and Planetary Systems*, eds. C. J. Lada & N. D. Kylafis (Kluwer), p227

Bally, J., Devine, D. & Reipurth, B. 1996, 473, L49

Bally, J. & Reipurth, B. 2001, *ARAA*, 39, 403

Bate, M. R., Bonnell, I. A., & Bromm, V. 2003, *MNRAS*, 339, 577

Boldyrev, S., Nordlund, A., & Padoan, P. 2002, *ApJ*, 573, 678

Bontemps, S., Andre, P., Tereby, S. & Cabrit, S. 1996, *AA*, 314, 477

Calvet, N. 1997, in *Herbig-Haro Flows in the Birth of Stars: IAU 182*, eds. B. Reipurth & C. Bertout (Kluwer Academic Publishers), p417

Caselli, P. & Myers, P. C. 1995, *ApJ*, 446, 665

Crapsi, A., Devries, C. H., Huard, T. L., et al. 2005, *AA*, 439, 1023

Crutcher, R. M. 1999, *ApJ*, 520, 706

Crutcher, R. M. 2005, in *Massive Star Birth: A Crossroads of Astrophysics*, IAU 227, eds. R. Cesaroni, M. Felli, E. Churchwell & C. M. Walmsley, (Cambridge University Press), p98

Davis, C. J., Matthews, H. E., Ray, T., Dent, W., & Richer, J. 1999, MNRAS, 309, 141

Elmegreen, B. C. 2006, in *Massive Stars: From Pop III and GRBs to the Milky Way*, eds. M. Livio and E. Villaver (Cambridge Univ. Press), in press (astro-ph/0610687)

Elmegreen, B. C. & Scalo, J. 2004, ARAA, 42, 275

Fridlund, C. & Liseau, R. 1994, AA, 292, 631

Froebrich, D., Smith, M. D., Hodapp, K.-W., & Eisloffel, J. 2003, MNRAS, 346, 163

Gueth, F., Guilloteau, S., & Bachiller, R. 1996, AA, 307, 891

Heitsch, F., Mac Low, M.-M., Klessen, R. S. 2001, ApJ, 547, 280

Houde, M., Dowell, C. D., Hildebrand, R. H., et al. 2004, ApJ, 604, 717

Kenyon, S. J. & Hartmann, L. 1995, ApJS, 101, 117

Klessen, R., Burkert, A., & Bate, M. R. 1998, ApJ, 501, L205

Knee, L. B. G. & Sandell, G. 2000, AA, 361, 671

Königl, A. & Pudritz, R. E. 2000, in *Planets and Protostars IV*, eds. V. Mannings, A. Boss, & S. Russell (Arizona: Univ of Arizona Press), p759

Krumholz, M. & McKee, C. F. 2005, ApJ, 630, 250

Krumholz, M. & Tan, J. 2006, ApJ, submitted (astro-ph/0606277)

Lada, C. J. 1985, ARAA, 23, 26

Lada, C. J., Alves, J., Lada, E. A. 1996, AJ, 111, 1964

Lada, C. J. & Lada, E. A. 2003, ARAA, 41, 57

Lada, E. A., Bally, J., & Stark, A. A. 1991, ApJ, 368, 432

Larson, R. B. 1981, MNRAS, 194, 809

Li, P. S., Norman, M. L., Mac Low, M.-M., & Heitsch, F. 2004, ApJ, 605, 800

Li, Z.-Y. & Nakamura, F. 2002, ApJ, 578, 256

Li, Z.-Y. & Nakamura, F. 2006, ApJ, 640, L187

Lucas, P. W. & Roche, P. F. 1996, MNRAS, 280, 1219

Mac Low, M.-M. 2000, ApJ, 524, 169

Mac Low, M.-M. 2000, in Star Formation from the Small to the Large Scale, eds. F. Favata, A. Kaas & A. Wilson (ESA SP445), p.457

Mac Low, M.-M., Klessen, R. S., Burkert, A., & Smith, M. D. 1998, Phys. Rev. Lett., 80, 2754

Matzner, C. D. 2007, ApJ, in press

Matzner, C. D. & McKee, C. F. 2000, ApJ, 545, 364

McKee, C. F. 1989, ApJ, 345, 782

Motte, F., Andre, P. & Neri, R. 1998, AA, 336, 150

Myers, P. C. & Fuller, G. A. 1993, ApJ, 402, 635

Myers, P. C. & Goodman, A. A. 1988, ApJ, 326, L27

Nakamura, F. & Li, Z.-Y. 2005, ApJ, 631, 411

Nakamura, F., Matsumoto, T., Hanawa, T., & Tomosaka, K. 1999, ApJ, 510, 274

Nakamura, F. 2000, ApJ, 543, 291

Nakano, T., Hasegawa, T. & Norman, C. 1995, ApJ, 450, 183

Nakano, T. & Nakamura, T. 1978, PASJ, 30, 681

Norman, C. & Silk, J. 1980, ApJ, 238, 158

Olmi, L. & Testi, L. 2002, AA, 392, 1053

Onishi, T., Mizuno, A., Kawamura, A., Tachihara, K. & Fukui, Y. 2002, ApJ, 575, 950

Ostriker, E. C., Gammie, C. F. & Stone, J. M. 2001, ApJ, 546, 980

Padoan, P. & Nordlund, A. 1999, ApJ, 526, 279

Peretto, N., Andre, P. & Belloche, A. 2006, AA, 445, 201

Richer, J. S., Shepherd, D. S., Cabrit, S., Bachiller, R., & Churchwell, E. 2000, in *Protostars and Planets VI*, eds. V. Mannings, A. Boss, & S. Russell (Arizona: Univ of Arizona Press), p867

Ridge, N. A., Wilson, T. L., Megeath, S. T., Allen, L. E. & Myers, P. C. 2003, *AJ*, 126, 286

Rodriguez, L. F., D'Alessio, P., Wilner, D. J., Ho, P. T. P., et al. 1998, *Nature*, 395, 355

Rodriguez, L. F., Porras, A., Claussen, M. J., et al. 2003, *ApJ*, 586, L137

Saito, H., Saito, M., Moriguchi, Y., & Fukui, Y. 2006, *PASJ*, 58, 343

Sandell, G. & Knee, L. 2001, *ApJ*, 546, L49

Schleuning, D. A. 1998, *ApJ*, 493, 811

Shang, H., Allen, A., Li, Z.-Y., Liu, C.-F., Chou, M.-Y., & Anderson, J. M. 2006, *ApJ*, 649, 845

Shu, F. H. 1977, *ApJ*, 214, 488

Shu, F. H., Allen, A., Shang, H., Ostriker, E. & Li, Z.-Y. 1999, in *The Origins of Stars and Planetary Systems*, eds. C. J. Lada & N. D. Kylafis (Kluwer), p193

Shu, F. H., Li, Z.-Y. & Allen, A. 2004, *ApJ*, 601, 930

Shu, F. H., Najita, J., Ostriker, E. & Shang, S. 1995, *ApJ*, 445, L155

Shu, F. H., Najita, J., Shang, H. & Li, Z.-Y. 2000, in *Planets and Protostars IV*, eds. V. Mannings, A. Boss, & S. Russell (Arizona: Univ of Arizona Press), p789

Snell, R., Loren, R. B. & Plambeck, R. L. 1980, *ApJ*, 239, L17

Stahler, S. W. 1988, *ApJ*, 332, 804

Stojimirovic, I., Narayanan, G., Snell, R. L., & Bally, J. 2006, *ApJ*, 649, 280

Stone, J. M., Ostriker, E. C., & Gammie, C. F. 1998, *ApJ*, 508, L99

Tilley, D. & Pudritz, R. 2004, *ApJ*, 353, 769

Umemoto, T., Iwata, T., Fukui, Y., Mikami, H., et al. 1992, *ApJ*, 392, L83

Vazquez-Semadeni, E., Kim, J., & Ballesteros-Paredes, J. 2005, *ApJ*, 630, L49

Vestuto, J. G., Ostriker, E. C., & Stone, J. M. 2003, *ApJ*, 590, 858

Walawender, J., Bally, J. & Reipurth, B. 2005, AJ, 129, 2308

Walsh, A. J., Bourke, T. L. & Myers, P. C. 2006, ApJ, 637, 860

Warin, S., Castets, A., Langer, W. D., Wilson, R., Pagani, L. 1996, AA, 306, 935

Williams, J. P. & Garland, C. A. 2002, ApJ, 568, 259

Williams, J. P. & Myers, P. C. 2000, ApJ, 537, 891

Wolf-Chase, G., Moriarty-Schieven, G., Fich, M. & Barsony, M. 2003, MNRAS, 344, 809

Zuckerman, B. & Evans, N. J. 1974, ApJ, 192, L149

7. APPENDIX: Protostellar Outflow Momentum

In this Appendix, we estimate a plausible range of the outflow momentum from several observations. Most, perhaps all, low-mass stars go through a phase of strong outflow during formation. The origin of the outflow is unclear. The leading scenario is that they are driven by rotating magnetic fields from close to the central object (e.g., Königl & Pudritz 2000; Shu et al. 2000). These winds interact with the environments that surround the forming stars, feeding energy and momentum back into the star-forming cloud. The best evidence for the wind-ambient interaction comes from bipolar molecular outflows (Lada 1985), which are thought to be the cloud material that has been set into motion by the interaction. Since the interaction is likely momentum (rather than energy) conserving, a useful quantity for characterizing the strength of the feedback is the total (time-integrated) momentum of the wind divided by the stellar mass, denoted by P_* (Matzner & McKee 2000). Its value can be constrained from both observations and theoretical considerations.

The best observational constraint on the wind momentum per unit stellar mass P_* comes from the famous source of bipolar molecular outflow, L1551 IRS5. The CO outflow is the first to be discovered (Snell et al. 1980), and remains arguably the best studied source (Stojimirovic et al. 2006). Just as importantly, the mass of its central object has been determined dynamically, based on radio observations of the orbital motions of the central binary system (Rodriguez et al. 2003); this mass is typically not available for other strong outflow sources, which are deeply embedded in general.

Stojimirovic et al. (2006) carried out a thorough study of the structure and kinematics of the outflow, and obtained a flow momentum between $20.5 - 26.5 M_{\odot} \text{ km s}^{-1}$ (depending on the excitation temperature adopted), corrected for the effects of CO optical depth but not inclination. The inclination angle i of the outflow to the plane of the sky is somewhat uncertain. Fridlund & Liseau (1994) found values ranging from $\sim 24^{\circ}$ to $\sim 43^{\circ}$ from the radial velocities and proper motions of HH knots that bisect the blue outflow lobe. Consistent with this range is the inclination angle ($i \sim 30^{\circ}$) for the symmetry axis of the system inferred from the modeling of IR images in scattered light (Lucas & Roche 1996) and continuum images of circumstellar disks at 7 mm (Rodriguez et al. 1998). If we adopt the same range for the molecular outflow as well, the inclination-corrected momentum would increase to $\sim 30.1 - 65.2 M_{\odot} \text{ km s}^{-1}$. This is likely a lower limit to the total momentum carried by the primary wind, because it does not include the contribution from the slowest part of the outflow (within 1.5 km/s of the systematic velocity) that is difficult to disentangle from the ambient cloud and there is evidence that the wind may have punched through part of the visible boundary of the L1551 cloud. Using the total stellar mass of $\sim 1.2 M_{\odot}$ for the binary estimated by Rodriguez et al. (2003), we find $P_* \gtrsim 25 - 54 \text{ km s}^{-1}$ for this particular source.

L1551 IRS5 is considered prototypical of moderately collimated, “classical” molecular outflows (Bachiller & Tafalla 1999). There is another class of highly collimated outflows, driven mostly by Class 0 objects. One of the best studied outflows in this class is L1157, driven by a low luminosity protostar of $\sim 11 L_{\odot}$ (Umemoto et al. 1992). Bachiller et al. (2001) obtained a total flow momentum of $4.71 M_{\odot} \text{ km/s}$, after correcting for the effects of CO optical depth but not inclination. A large inclination correction factor is needed, since the outflow appears to lie close to the plane of the sky. If one adopts the value $i \sim 9^{\circ}$ deduced by Gueth et al. (1996), the momentum would increase by a factor of 6.4, to $\sim 30 M_{\odot} \text{ km/s}$. The mass of the central object is uncertain. For a rough estimate, we assume that most of the bolometric luminosity L_{bol} comes from the accretion luminosity

$$L_{\text{acc}} = \frac{G \dot{M}_* M_*}{R_*} \quad (12)$$

and that the mass accretion rate \dot{M}_* is given by M_*/t_{dyn} , where M_* is the stellar mass and t_{dyn} is the dynamical time for the outflow, which is measured to be $\sim 3 \times 10^4$ years for L1157 (Bachiller et al. 2001). Under these assumptions, we find

$$M_* \approx \left(\frac{L_{\text{bol}} R_* t_{\text{dyn}}}{G} \right)^{1/2} = 0.17 \left(\frac{L_{\text{bol}}}{10 L_{\odot}} \right)^{1/2} \left(\frac{R_*}{3 R_{\odot}} \right)^{1/2} \left(\frac{t_{\text{dyn}}}{3 \times 10^4 \text{ yrs}} \right)^{1/2} M_{\odot}, \quad (13)$$

where the radius R_* of the (low-mass) protostar should be within a factor of 2 of the scaling $3 R_{\odot}$ (Stahler 1988). Froebrich et al. (2003) estimated a somewhat lower stellar mass ($0.1 M_{\odot}$)

for L1157, adopting a more elaborate, time dependent model for mass accretion and a lower $L_{\text{bol}} = 7.6 \pm 0.8 L_{\odot}$. These crude estimates, if not too far off the true value, would point to a large value for the wind momentum per unit stellar mass P_* of more than 10^2 km/s for this particular case.

The above values of P_* estimated for the best studied cases may not be representative, however. They are likely biased toward high values because of observational selection effects; weaker outflows are more difficult to study in detail. To account for the possibility of a range of values for P_* , we introduce a dimensionless parameter

$$f = \left(\frac{P_*}{100 \text{ km/s}} \right) = \left(\frac{V_w}{10^2 \text{ km/s}} \right) \left(\frac{M_w}{M_*} \right). \quad (14)$$

It is the product of the speed of the primary wind V_w in units of 10^2 km/s and the fraction of the stellar mass that is ejected in the wind. For revealed T Tauri stars where the wind speed can be measured directly, V_w is typically a few hundred km/s. In the X-wind theory (Shu et al. 2000), the most natural value for the ratio M_w/M_* is $\sim 1/3$. It is therefore conceivable that f may be as high as unity. Some support for a relatively high value of f comes from the unpublished work of Cabrit & Shepherd (quoted in Richer et al. 2000), which indicates that $(M_w V_w)/(M_* V_K) \sim 0.3$ (where $V_K = [GM_*/R_*]^{1/2}$ is the Keplerian speed at the stellar surface) over a wide range of stellar luminosity. For a typical young star of mass $M_* \approx 0.5 M_{\odot}$ and radius $R_* \approx 3 R_{\odot}$, we have $P_* \sim 0.3 V_K \approx 53$ km/s (or $f \approx 0.5$). On the other hand, the wind during the deeply embedded phase (when most of the driving of molecular outflows occurs) may be somewhat slower, both because of a smaller stellar mass (and thus a shallower gravitational potential well) and because of a likely higher wind mass loading which, in the magnetocentrifugal wind theory, would lead to a slower outflow (e.g., Anderson et al. 2005). Also, there is evidence that the ratio of mass loss rate in the wind and accretion rate onto the star $\dot{M}_w/\dot{M}_* \approx 0.1$ during both the revealed (Calvet 1997) and the embedded phase (Bontemps et al. 1996). These estimates, although fairly uncertain, point to values for f as low as ~ 0.1 .

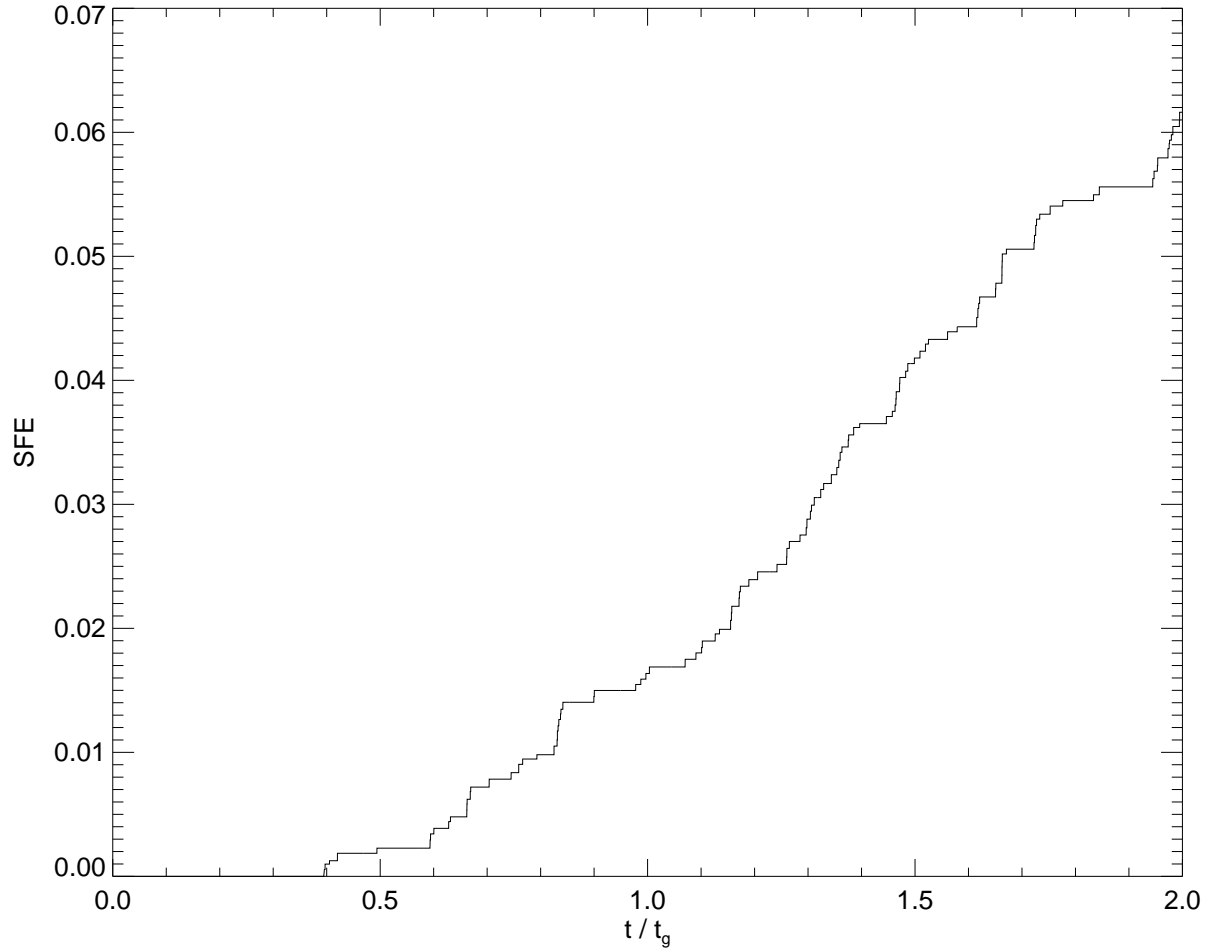


Fig. 1.— Evolution of the star formation efficiency (SFE) in the standard model (Model S0), showing that only a few percent of the gas is converted into stars per free-fall time ($\bar{t}_{\text{ff}} = 0.79 t_g$).

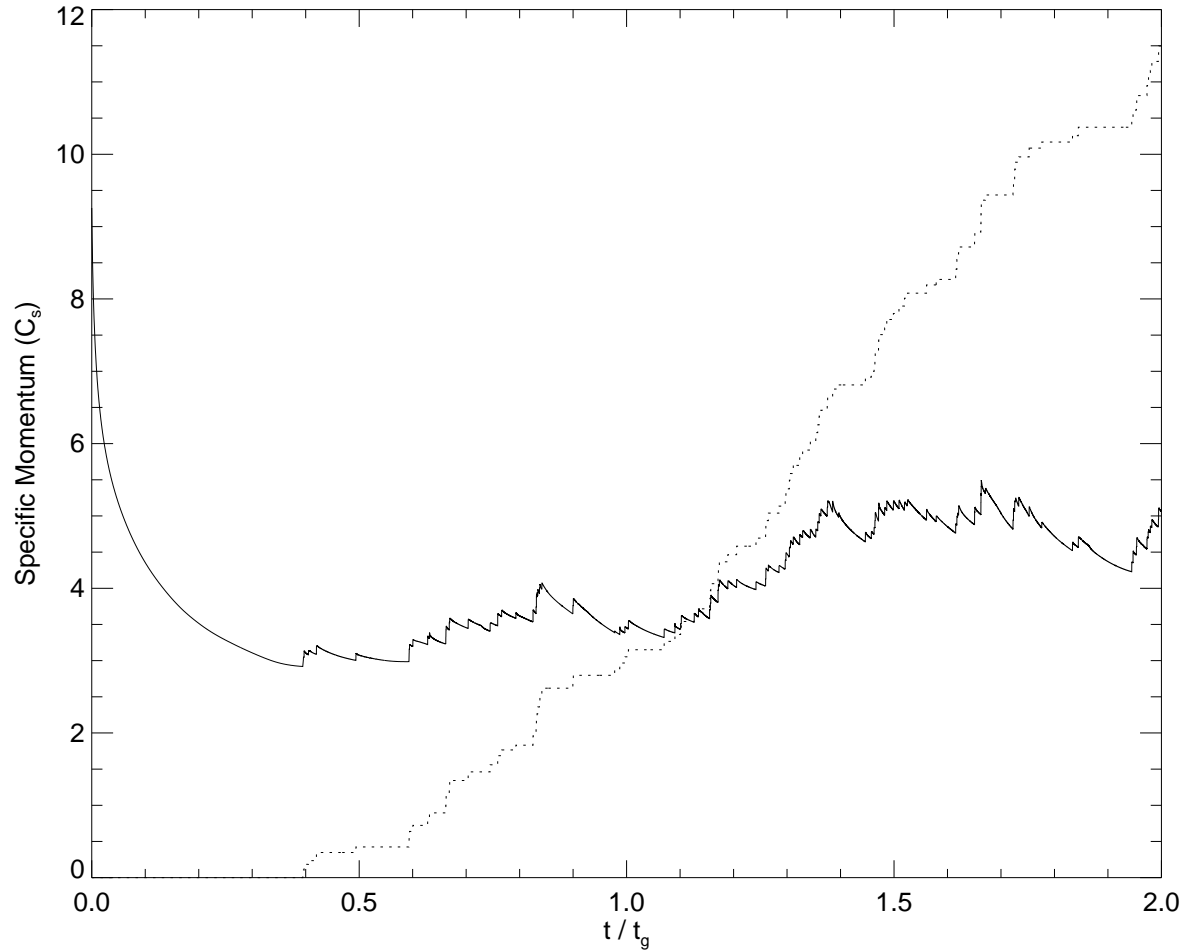


Fig. 2.— Comparison of the specific (scalar) momentum v_{turb} (solid line) in the turbulent cluster-forming clump at a given time and the amount of specific momentum v_{inj} (dotted) injected into the clump by outflows up to that time.

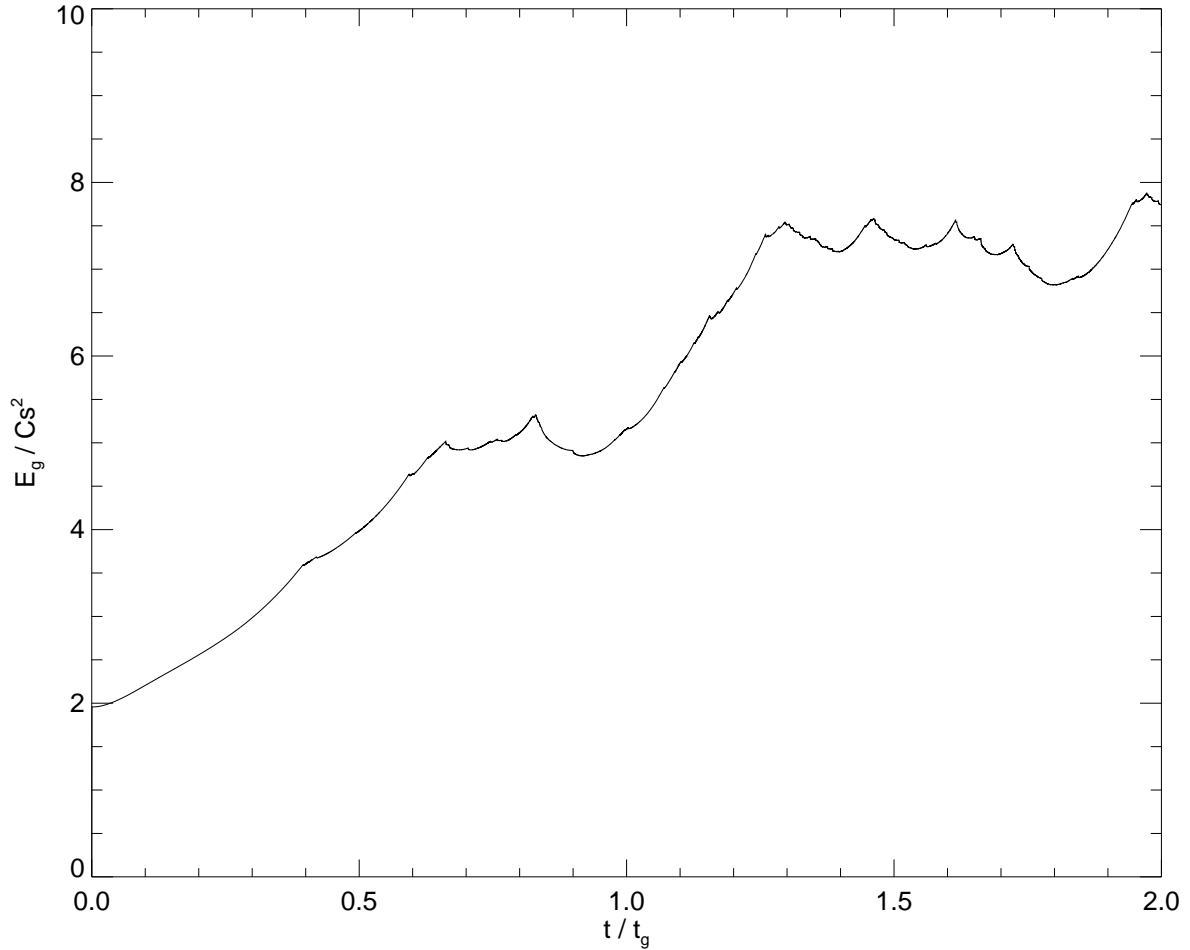


Fig. 3.— Evolution of the absolute value of the gravitational energy per unit mass. The energy becomes nearly constant at late times, signaling that a quasi-equilibrium state has been reached.

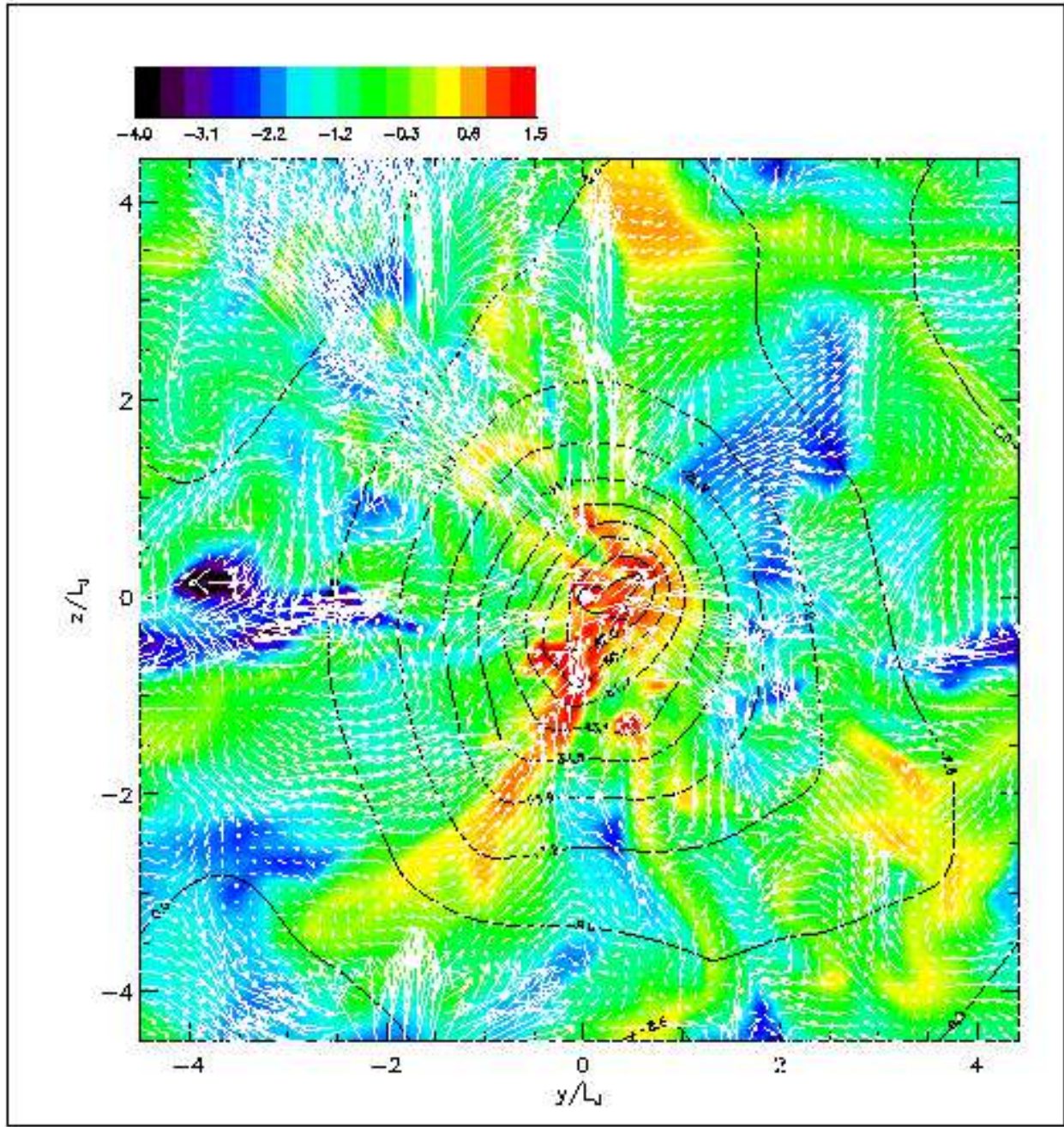


Fig. 4.— A slice through the standard simulation in the y - z plane. The color map is for the logarithm of the density $\log(\rho/\rho_0)$, arrows for the velocity vectors and contours for the gravitational potential. The contours are plotted at 0.0, 0.1, ..., 0.9 times the minimum value of the potential ($-86.2 c_s^2$). For clarity, the length of velocity vector is capped at $15 c_s$ and the location of minimum gravitational potential is shifted to the center of the map.

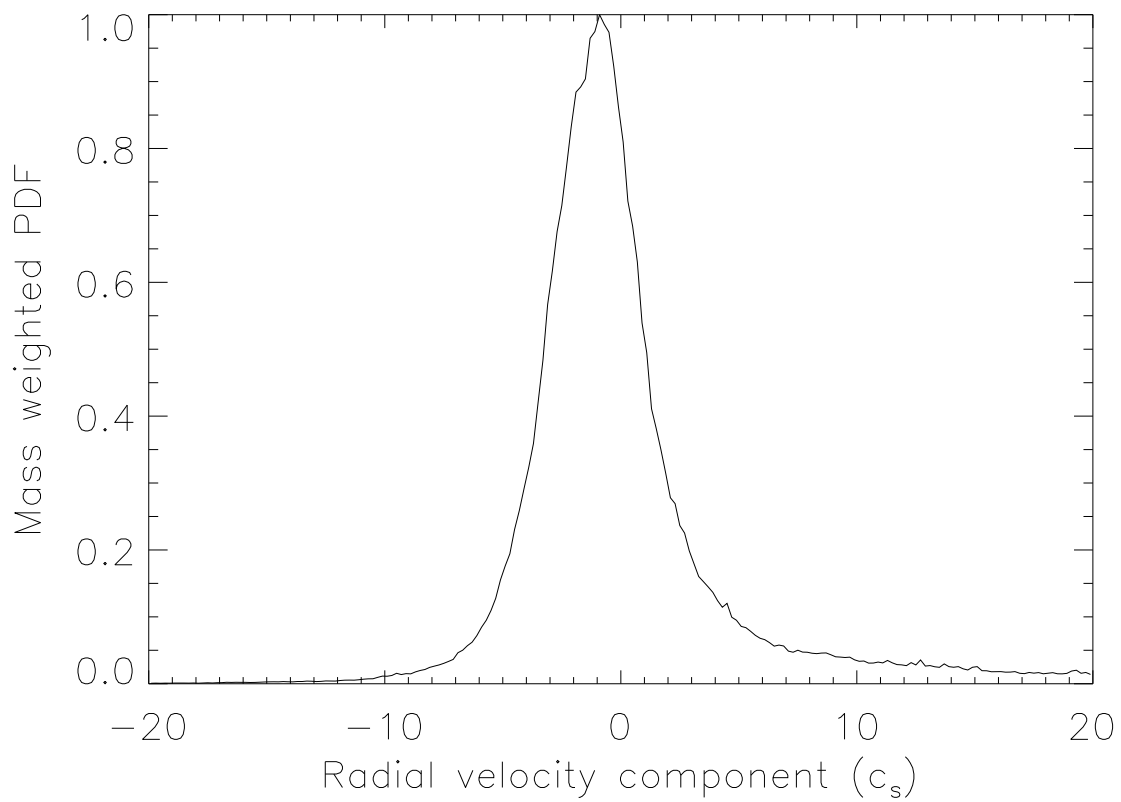


Fig. 5.— Mass weighted PDF for the radial velocity component. The maximum of the distribution is normalized to unity.

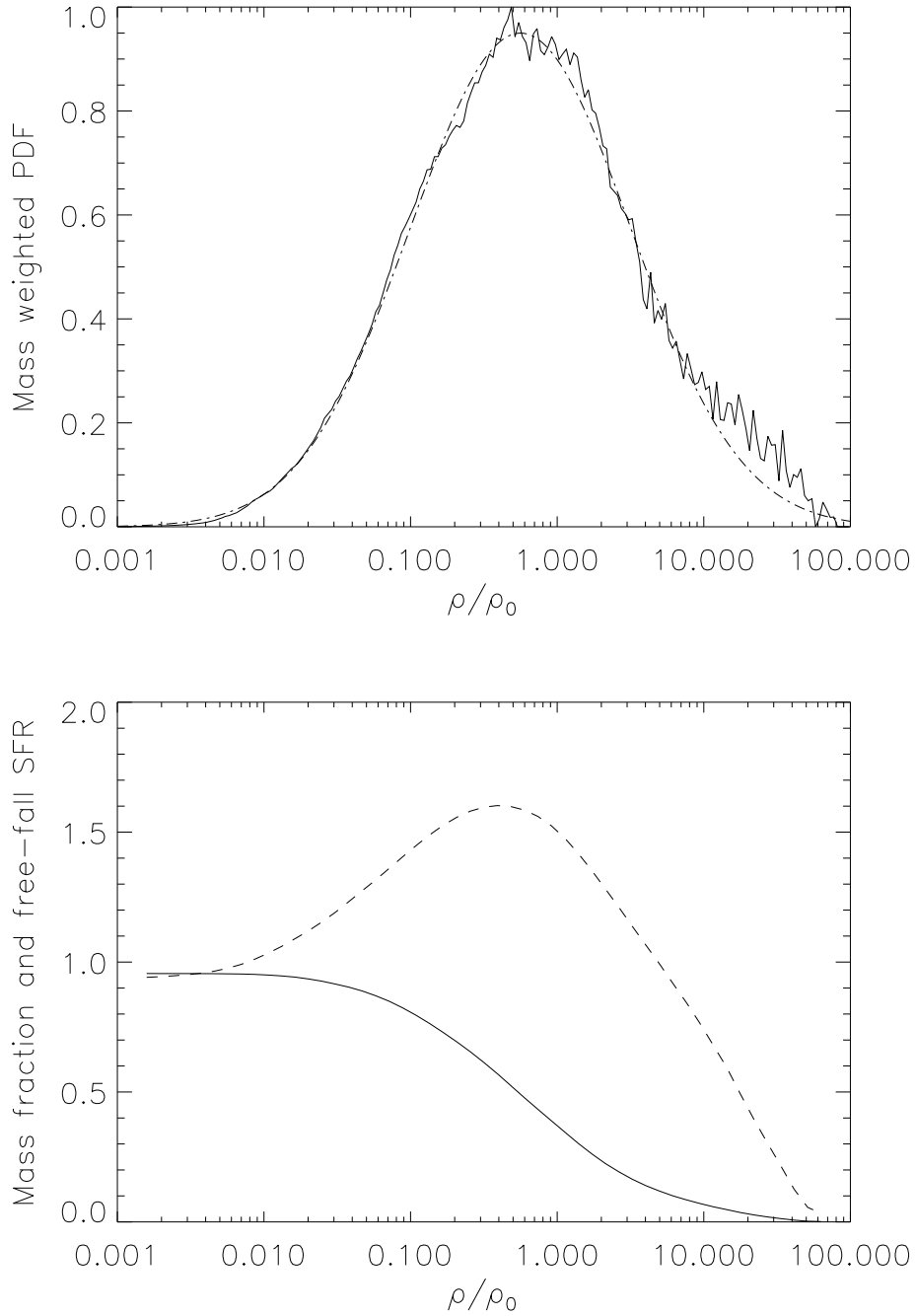


Fig. 6.— (a) Mass weighted probability distribution function (PDF) for the volume density (solid line). Also plotted is a fitted lognormal distribution for comparison. (b) The accumulative mass fraction (solid) and the limiting (free-fall) rate of star formation (dashed) for the gas above a given density.

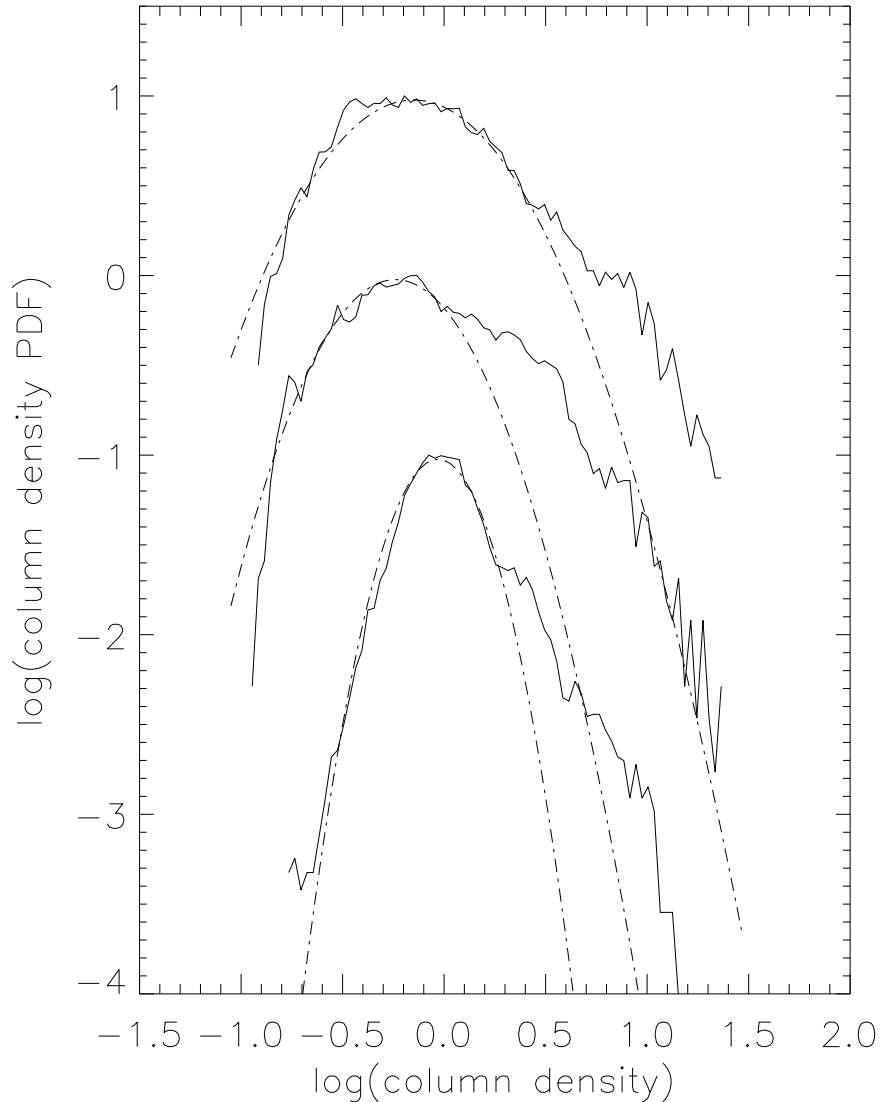


Fig. 7.— Probability distribution functions (PDFs) of the column density (in units of $\rho_0 L_J$) along the x - (bottom), y - (middle) and z -axis (top). The curves are offset for clarity, with fitted lognormal distributions (dash-dotted lines) superposed for comparison.

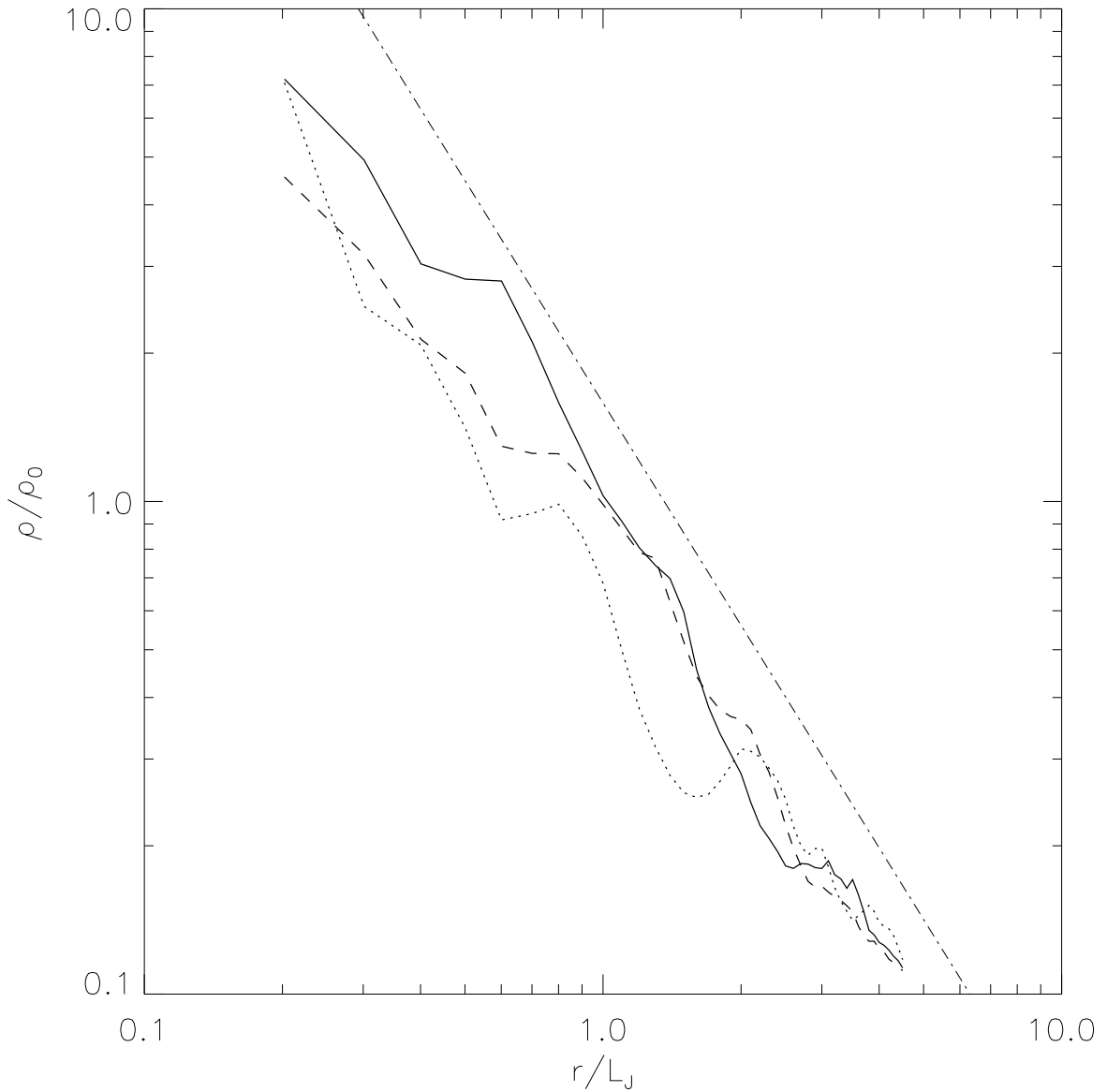


Fig. 8.— Distributions of the spherically averaged density as a function of radius at the representative times $t=1.0$ (dashed), 1.5 (solid) and 2.0 t_g (dotted). A power-law $\rho \propto r^{-1.5}$ (dash-dotted line) is shown for comparison.

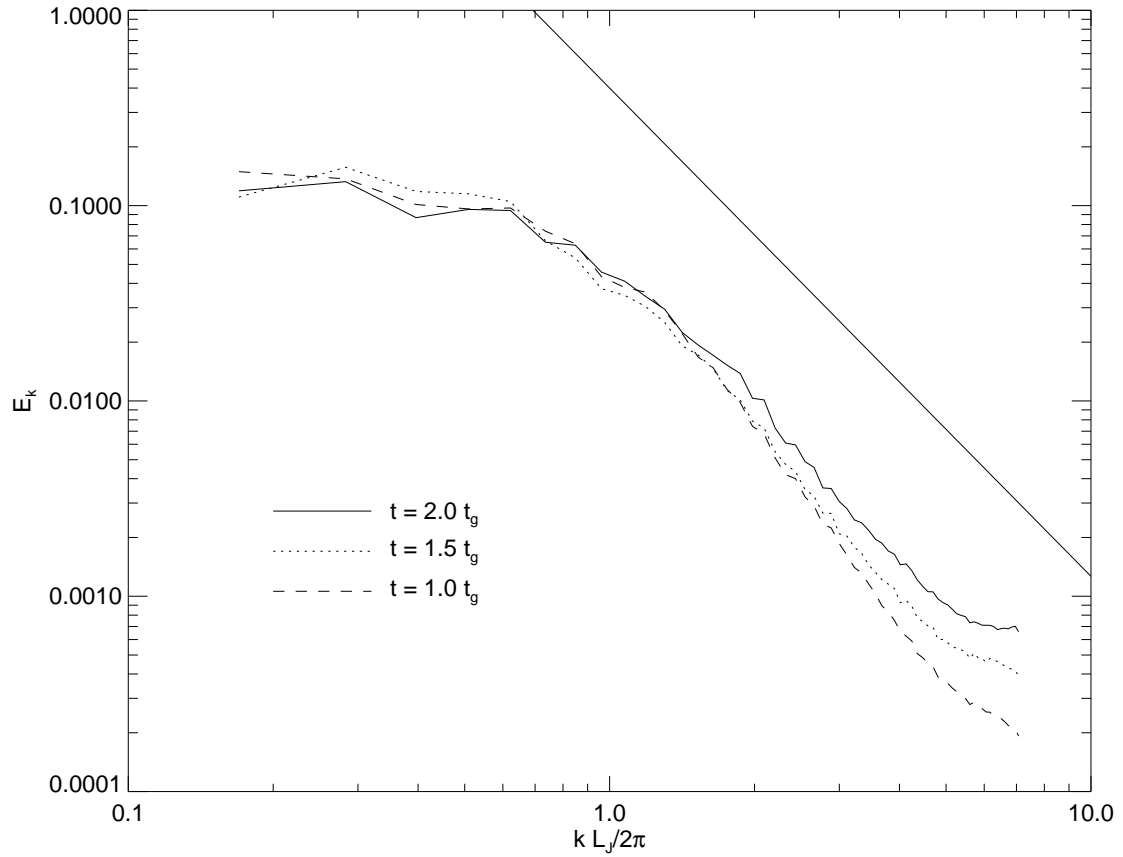


Fig. 9.— Normalized velocity power spectra $E_k = k^2 v_k^2$ of the protostellar turbulence at three representative times 1.0 (dashed), 1.5 (solid) and 2.0 t_g (dotted). Also shown for comparison is a power-law $E_k \propto k^{-2.5}$ (straight solid line).

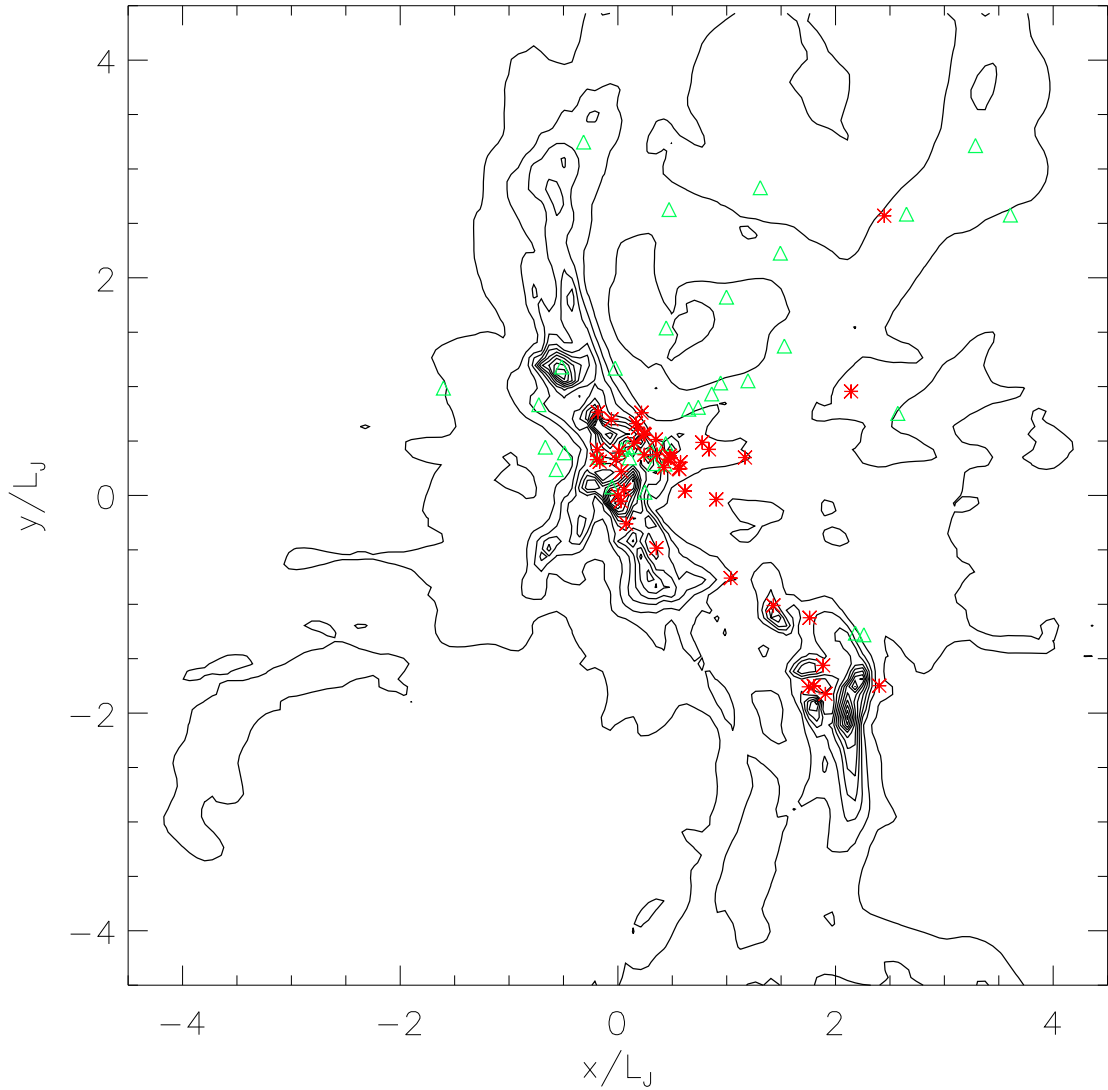


Fig. 10.— Spatial distributions of the stars and gas at the representative time $1.5 t_g$. Stars formed before $1 t_g$ are denoted by green triangles, and those after $1 t_g$ by red asterisks. The contours are for the column density in units of $\rho_0 L_J$, starting from 1 and increasing in increments of 2.

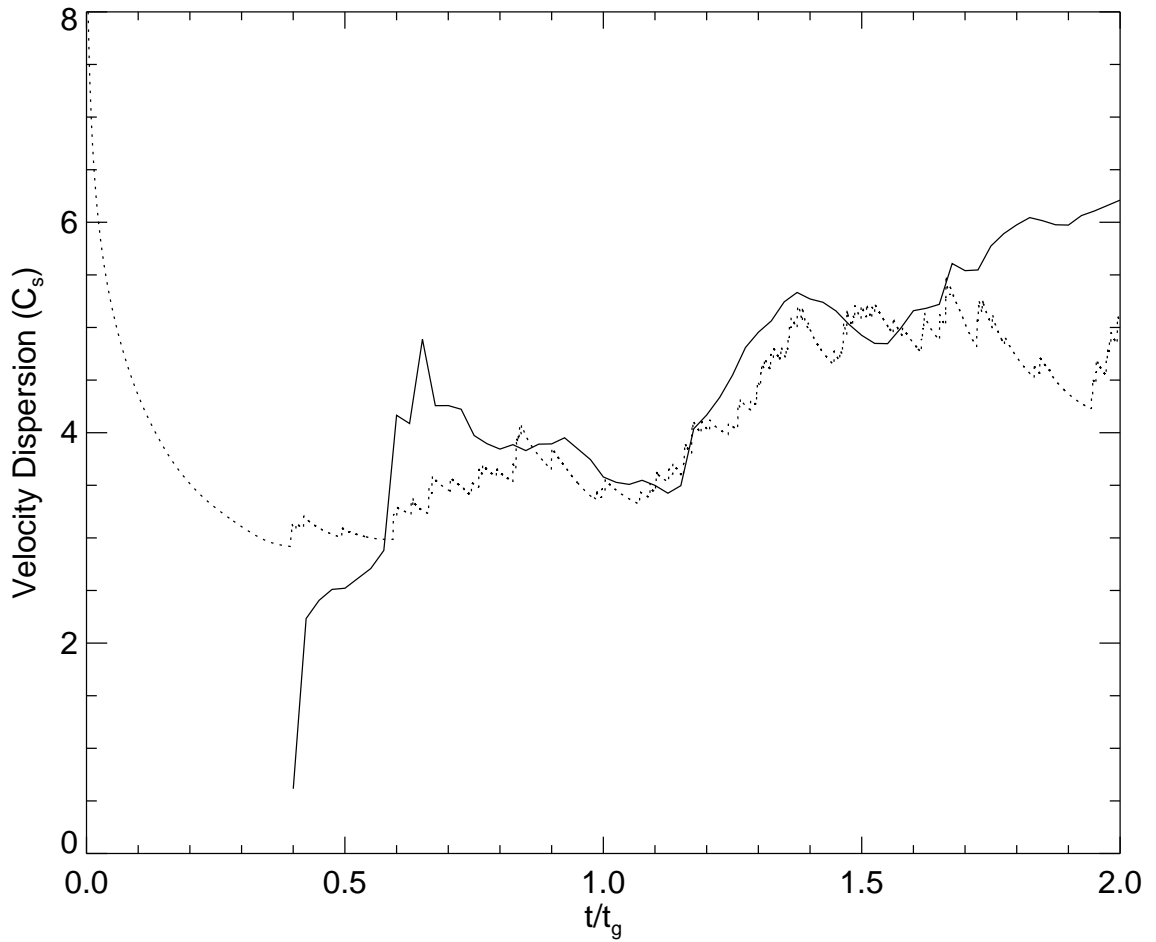


Fig. 11.— Evolution of the stellar velocity dispersion σ_* (solid line). Also plotted for comparison is the mass-weighted turbulent speed of the gas v_{turb} (dotted).

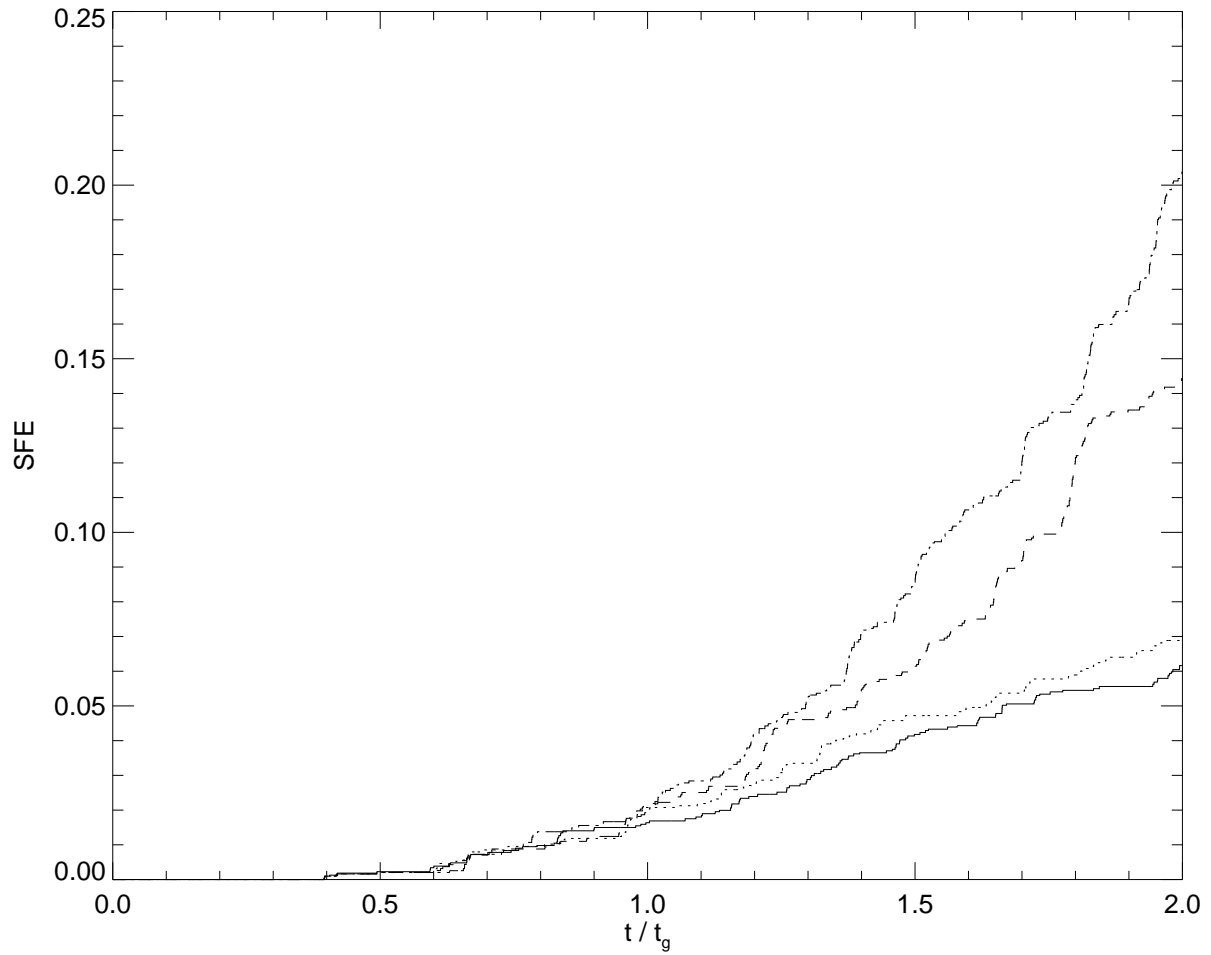


Fig. 12.— SFEs for collimated and spherical outflow models. The upper most curve is for the spherical model (dash-dotted, Model E1), while the lower curves are for models of collimated outflows with a jet momentum fraction $\eta = 0.25$ (dashed, Model E2), 0.50 (dotted, Model E3) and 0.75 (solid, standard Model S0) respectively.



Fig. 13.— The same as Fig. 7 but for the spherical outflow model (Model E2) at the time $2t_g$.

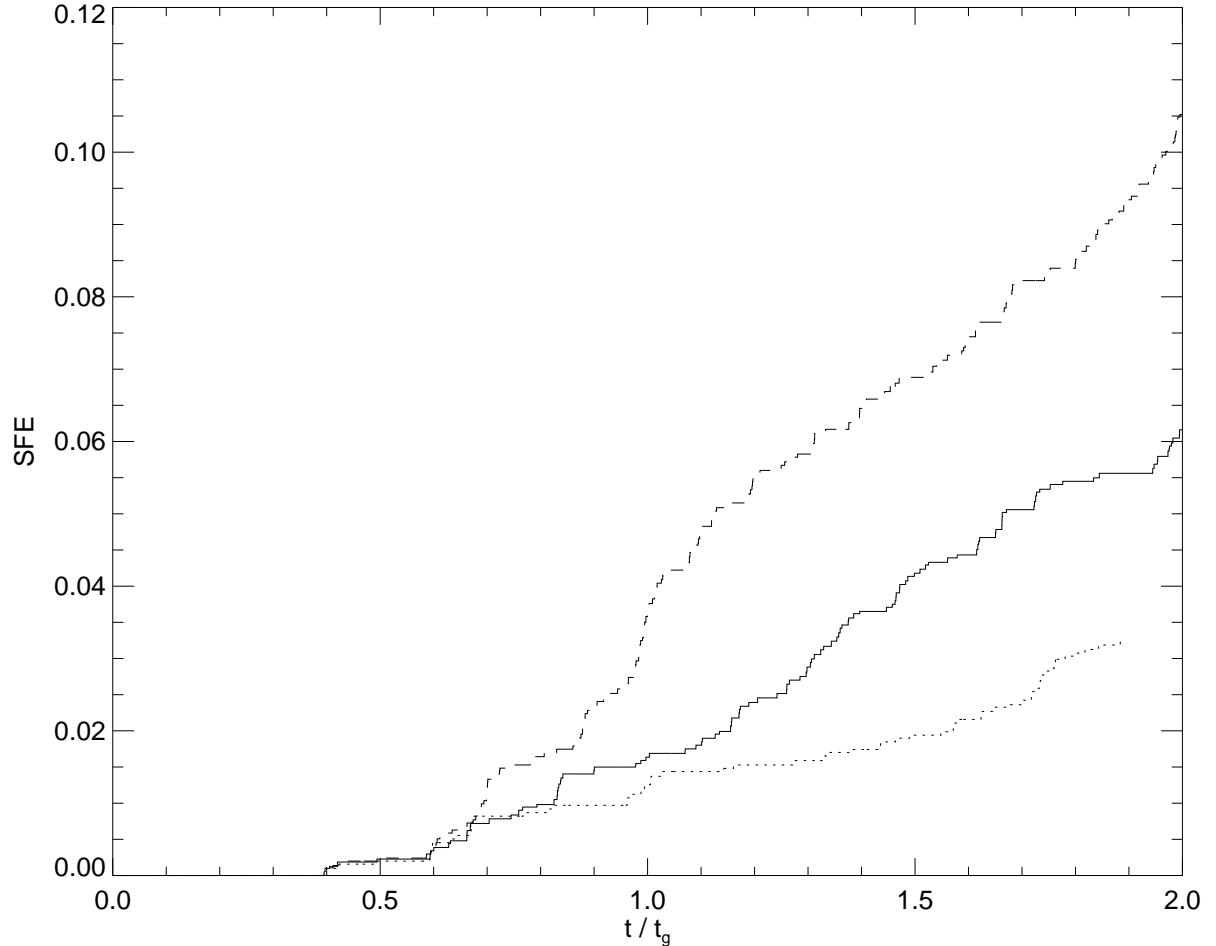


Fig. 14.— Upper panel: SFEs for models of different outflow strengths. The curves are for the cases with outflow parameter $f = 0.25$ (dashed, Model F1), 0.50 (solid, standard Model S0) and 0.75 (dotted, Model F2) respectively. Lower panel: Products of SFE and f , showing that the total momentum injected into the cloud is insensitive to the outflow strength.

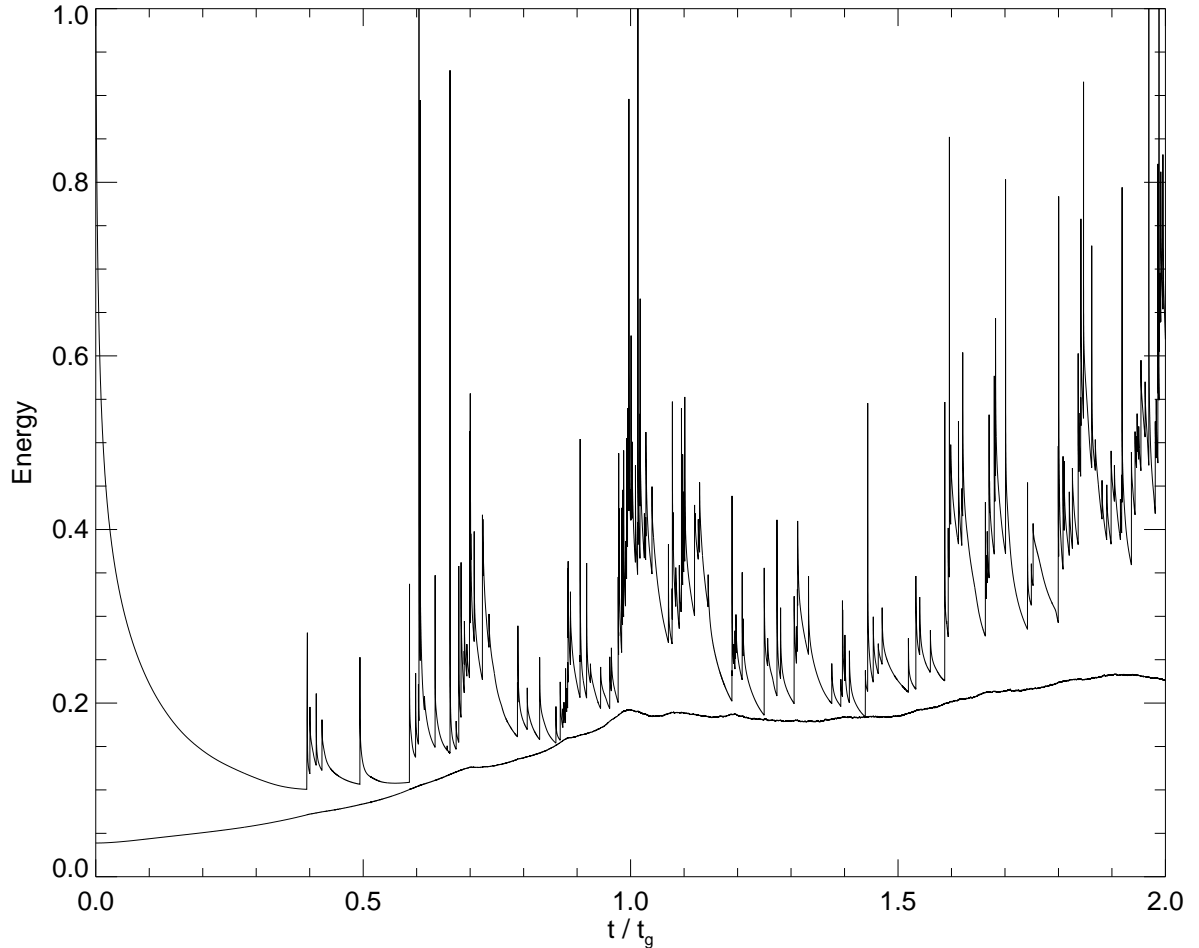


Fig. 15.— Evolution of the kinetic and gravitational energies of the gas in Model F1 with relatively weak outflows ($f = 0.25$). The energies are normalized by the initial kinetic energy of the turbulence, which is $50 c_s^2$ per unit mass, corresponding to a mass-weighted rms Mach number of 10.

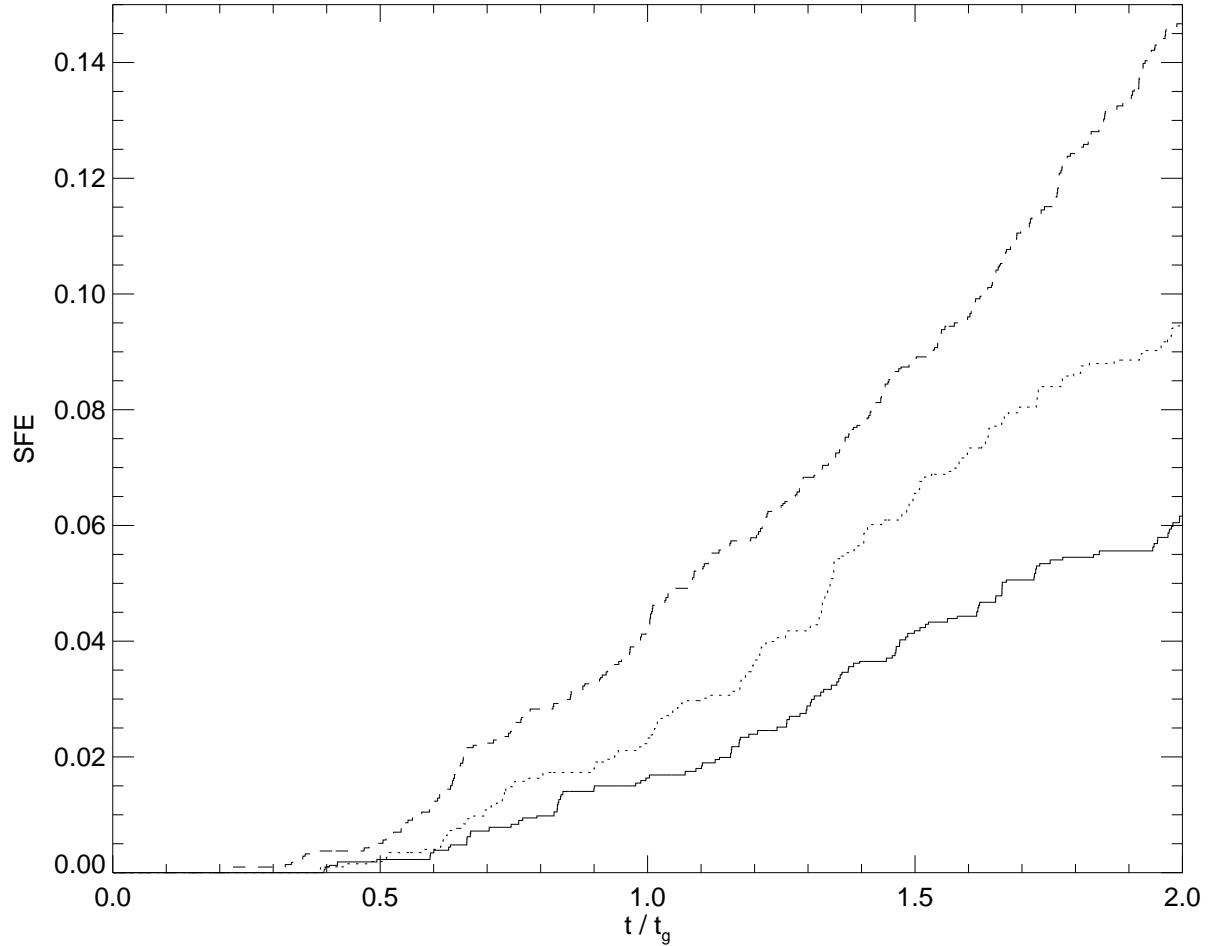


Fig. 16.— SFEs for models of different magnetic field strengths. The curves are for the cases with $\alpha = 10^{-6}$ (dashed, Model M1), 0.5 (dotted, Model M2) and 2.5 (solid, standard Model S0) respectively.

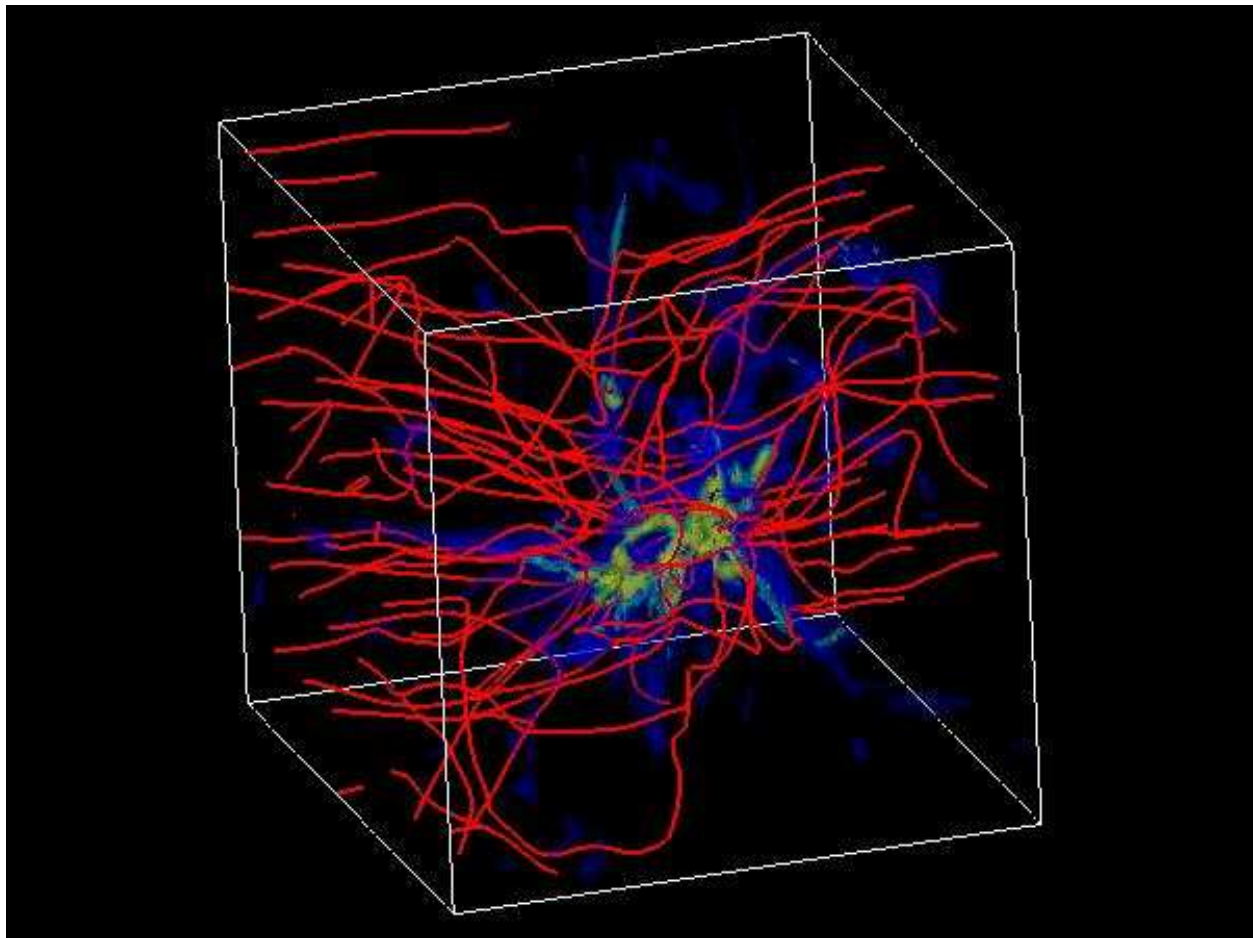


Fig. 17.— Magnetic field lines and density distribution in 3D for Model M2 ($\alpha = 0.5$). The field lines are drawn in red. The blue and yellow isodensity surfaces are for 1 and $30 \rho_0$ respectively.

Table 1. Model Parameters

Model	α	f	η	Note
S0	2.5	0.5	0.75	standard model, with jet component
E1	2.5	0.5	n/a	spherical outflow, no jet component
E2	2.5	0.5	0.25	significantly weaker jet component
E3	2.5	0.5	0.50	somewhat weaker jet component
F1	2.5	0.25	0.75	weaker outflow
F2	2.5	0.75	0.75	stronger outflow
M1	10^{-6}	0.50	0.75	extremely weak magnetic field
M2	0.5	0.5	0.75	weaker magnetic field

Note. — The quantity α is the ratio of magnetic to thermal pressure at the cloud center, f the dimensionless parameter for outflow strength, and η the fraction of outflow momentum carried in the jet component. All models are run to $2 t_g$, except for Model F2, which is terminated around $1.8 t_g$ because the time step becomes prohibitively small.